POLITECNICO DI TORINO

Corso di Laurea in Ingegneria Elettronica/Electronic Engineering
Devices and Technologies for Integrated Electronics and
Optoelectronics

Tesi di Laurea Magistrale

Temperature-dependent rate equation model for high-speed vertical-cavity surface-emitting lasers

Supervisors
Dr. Alberto Tibaldi
Dr. Pierluigi Debernardi
Prof. Michele Goano
Prof. Roberto Gaudino

Candidate
Giuseppe Pio Pisa

Company Supervisor
Dr. Roger King

DICEMBRE 2020

Alla mia famiglia

Acknowledgements

Summary

In recent years, seventeen billion devices worldwide have been connected to internet. This number is going to increase year by year. In addition, the complexity and the quality of the services offered to the users grows incessantly. One needs only to think, for example, that many platforms, such as Youtube, offer 4K videos, a much higher quality than that proposed years ago. As most of this information traffic is generated and processed in data centers, they need ever more performing hardware. The spread of cloud computing is another important factor contributing to the growth of the data center market. Many big companies such as Google, Facebook and Amazon invested heavily to create an optimized and high-performing data center network. So in light of this, short-range communication plays a crucial role for intra-datacenter links. They require low cost, low power and high-speed transmitters; all requirements met by vertical-cavity surface-emitting lasers (VCSELs).

The design and the optimization of a VCSEL is not an easy task since different, strongly coupled, physical phenomena take place in the whole device and they determine its operation. A complete and accurate treatment would require the solution of three main problems: electrical, optical and thermal. Complex numerical models are needed to reach such accuracy but they are time-consuming, hence unsuited to simulate thousands of bits. The scope of this thesis is to implement a simple and fast model that takes into account all three phenomena providing indications of the performance-limiting factors and, possibly, suggesting optimizations and improvements. The idea is to start from the commonly adopted rate equations, modelling electro-optical interaction, and to introduce a simple model for the temperature, relevant in such devices. A good thermal characterization is important since VCSELs require large bandwidth over the entire operating range and the temperature affects their performance. This work has been conducted in collaboration with the industrial partner TRUMF Photonic Components GmbH (a company based in Ulm, Germany, that designs and produces VCSELs).

The thesis is organized as follows:

- Chapter 1 describes VCSELs operation, structure and performance.

- Chapter 2 introduces, firstly, the simplest, commonly adopted, rate equation model without any temperature-dependence. Its analytical solution is derived

in view of obtaining relevant figures of merit. As a second step, the temperature is introduced statically in the proceeding rate equation analysis with a simple model based on a thermal resistance. Then, it is analysed the thermal effect on the rate equation parameters. A particular attention is given to the numerical algorithm implemented.

- In chapter 3 the numerical model is applied to a real device provided by the industrial partner TRUMPF. Simulation parameters are fitted in order to match the measured results.

Contents

List of Tables

List of Figures

List of Abbreviations

VCSEL	vertical-cavity surface-emitting laser	**MMF**	multi-mode optical fiber
CAGR	compound annual growth rate	**E-O**	electrical-to-optical
		BER	bit error rate
DH	double-heterostructure	**NRZ**	non-return-to-zero
QW	quantum well	**DSP**	digital signal processing
DBR	distributed Bragg reflector	**LiDAR**	light-detection-and-ranging
MOCVD	metal-organic chemical vapor deposition	**VENUS**	Vcsel Electro-opto-thermal NUmerical Simulator
MBE	molecular beam epitaxy		
LW-VCSEL	long-wavelength VCSEL	**LI**	light-to-current
BTJ	buried tunnel junction	**VI**	voltage-to-current
POF	polymer optical fiber	**LUT**	look-up table
EEL	edge-emitting laser	**PL**	photoluminescence
DFB	distributed feedback laser	**ODE**	ordinary differential equation
LED	light-emitting diode		

Chapter 1

Introduction

1.1 VCSELs

A VCSEL is a type of semiconductor laser diode that emits light perpendicularly to the semiconductor wafer surface. In the late 1970s a huge contribution on VCSELs operation was done by Soda, Iga, Kitahara and Suematsu [1], but only in 1988 devices for CW operation were reported. In 1996, Honeywell was the first company to commercialize VCSEL technology [2]. First generation VCSELs, mainly, was made from GaAs-AlGaAs compound semiconductor relying on proton implantation for emission around 850 nm [3]. Nowadays VCSELs are widely used in several applications, including Face ID [4], smart-glasses [5], optical mouse and fiber interconnections. The global VCSEL market is rising at a compound annual growth rate (CAGR) of 31% from $0.738bn in 2018 to $3.775bn in 2024. The smartphone industry drives this higher rate of growth: today, up to three VCSELs dies can be integrated in a single smartphone as proximity, front and rear 3D sensor.

1.2 VCSEL: principle of operation

The principle of operation of a VCSEL is the same of a common laser. The main building blocks are an active medium, a pumping mechanism and an optical resonator. A basic laser system is shown in Figure 1.1.

   The optical resonator consists of a cavity sandwiched between two reflectors who provide optical feedback. The optical field in the cavity

1. is first reflected at the left facet

2. then propagates towards rigth for the whole cavity length

3. is reflected at the right facet

4. finally propagates toward left for the whole cavity length.
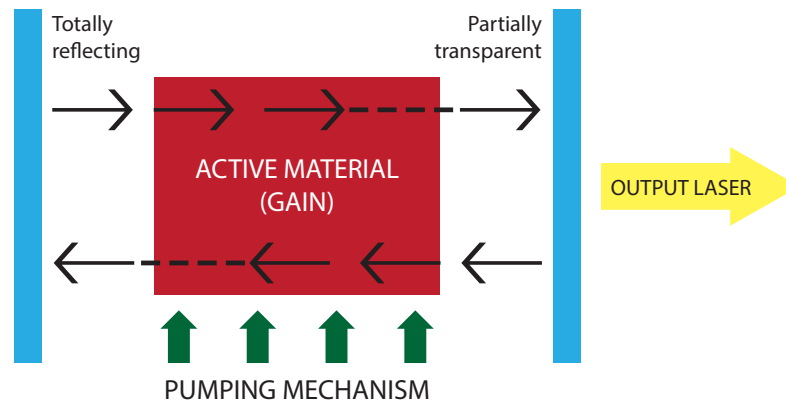
Figure 1.1.   Basic laser scheme.

This cycle represents a single round trip but the optical field continuously jumps back and forward in the cavity. Clearly, assuming no losses, in the steady-state regime a field is present in the cavity only if it sums in phase every round trip. The last condition sets the modes in the cavity that are able to lase. The optical resonator just described is the so called 'Fabry-Perot' resonator.

In a real device, lasing modes amplitude decreases each cycle due to losses: an active medium that provides gain is necessary to amplify the optical field in order to have in the steady-state regime a constant oscillation. The pumping mechanism gives the energy for this amplification. In a semiconductor laser such as VCSEL, optical gain is achieved through the process of stimulated emission. An incident photon in the active region induces the recombination of an electron-hole pair that generates a new photon, with the same energy and phase of the incident one. Therefore, an injection of electrons and holes must be provided to replace the carriers involved in the process of the stimulated emission. In modern diode laser, the pumping mechanism is achieved by a double-heterostructure (DH) able to confine carriers (Figure 1.2). An intrinsic layer with lower bandgap is placed between a p- and n- cladding layers, which have higher bandgap. Electrons and holes, injected by the external electric field, are captured in the intrinsic layer where they recombine creating photons with energy equal to the lower bandgap material. Since the bandgap of the cladding layer is larger, the light generated in the active region can not be absorbed in them and it is coupled out through one of the two facets.

1.3   VCSEL structure

A common VCSEL structure is shown in Figure 1.3. The lasing cavity consists of one or more quantum wells (QWs) placed between two distributed Bragg reflectors (DBRs) which provide optical feedback. DBRs consists of layers, whose thickness
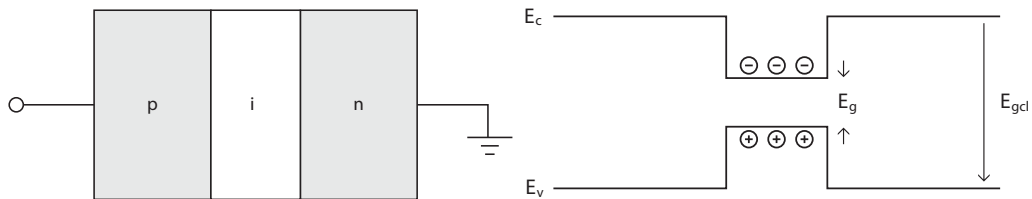
Figure 1.2. Left: DH structure. Right: the corresponding band diagram.

is quarter of the laser wavelength in the material, alternating lower and higher refractive indices. Typically more than 20 semiconductor layer pairs are needed for each mirror to reach a very high reflectivity ($\approx 99\%$) required to balance the short amplification length.

Due to the geometry of the structure, epitaxial growth is used to create each layer. Typical techniques employed for crystal growth are metal-organic chemical vapor deposition (MOCVD) and molecular beam epitaxy (MBE).

Generally, a PIN-type diode configuration is used: p-type and n-type materials, respectively, for upper and lower mirrors. A p-on-n doping is preferred to n-on-p doping on a n-type substrate to minimize crystal defects.

Electrical pumping can be achieved contacting both mirrors with a metallic electrode. The top one has a circular shape to allow the coupling of the light.

The structure analysed achieves longitudinal optical confinement thanks to the presence of the two DBRs. In order to have a low divergent circular beam at the output, current confinement and transverse optical confinement must be ensured. Several techniques have been used to this aim: mesa-etching of the top mirror [6], proton implantation [7] and selective lateral oxidation [8]. Figure 1.4 shows the three techniques. Mesa-etching exposes the active region to air causing reliability problems. Proton implantation has been the first technique used but it exhibits unstable, current-dependent beam characteristic since there is no built-in index guide: transverse optical confinement relies on thermal lensing. On the contrary oxide VCSELs cover, nowadays, the whole market. Selective layers are oxidized through wet-chemical oxidation creating a non-conducting lateral region that forces the current to be injected in the central region. Oxidation lowers the refractive index of the lateral region (from ≈ 3 to ≈ 1.6) creating a guiding effect that guarantees a good optical confinement.

1.4   Material for VCSELs

VCSELs operating wavelength is determined by the bandgap of the active material in the QWs. The most mature technology includes VCSELs operating at 850 nm, the standard wavelength used for short-range fiber communication, whose active
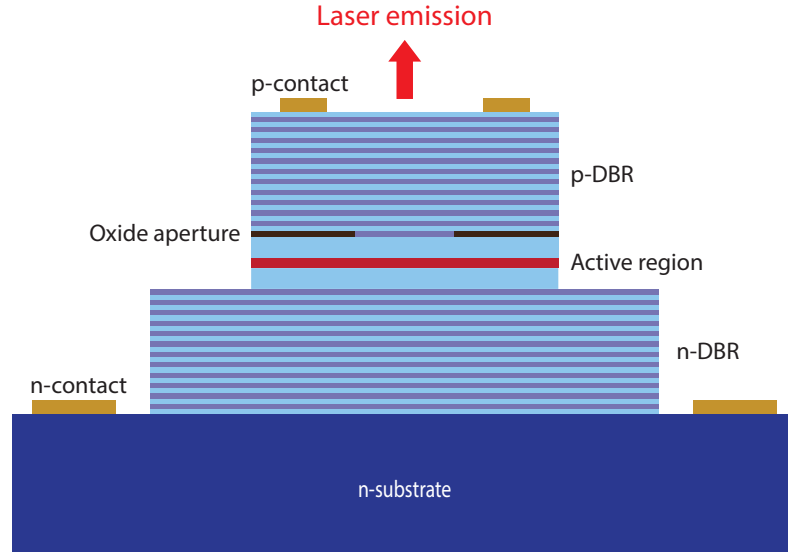
Figure 1.3.   VCSEL structure.
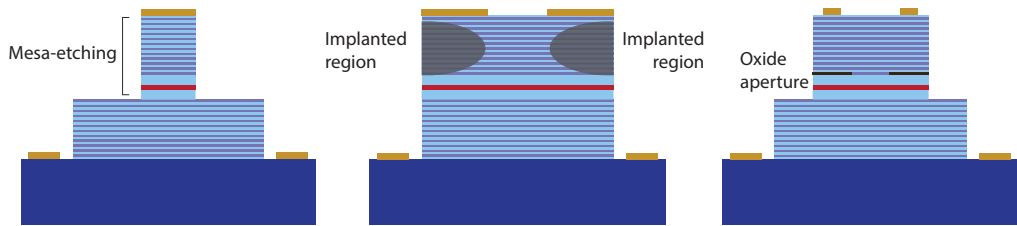
Figure 1.4.   Current confinement technique in VCSELs.   From left to right: mesa-etching, proton implantation, oxidation.

region is generally based on GaAs/AlGaAs and InGaAs/AlGaAs designs. They can be easily grown on GaAs substrate reducing significantly crystal defects that lower the performance.

The presence of a little amount of Indium in the GaAs region (typically $\approx 10\%$) introduces some strain that can double the achievable gain and the differential gain enhancing the performance with respect to the unstrained QWs. Playing with the percentage of Indium is possible to increase the operating wavelength reaching 980 nm and 1.1 μm.

During the past, an intense work has been done on long-wavelength VCSELs (LW-VCSELs) that cover a regime above 1.3 μm. They need an InP-based active region (InGaAsP or InGaAlAs) that cannot be grown unfortunately on GaAs substrates. While short-wavelength VCSELs based on GaAs-AlGaAs usually relies on lateral photon and current confinement via oxidized Al(Ga)As, other technologies

4

have to be applied for InP. A promising solution is represented by the wafer fusion technique [9] where the InP-based active region is fused to the GaAs-mirror structure. Devices based on the previous technique have not been commercialized. Nowadays, commercial InP VCSELs are based on a buried tunnel junction (BTJ) for current confinement in conjunction with a DBR [10].

In application where pointing, display and scanning are relevant, visible VCSELs below 700 nm are used. They are based on a AlGaInP system [11], whose aluminium content increases the bandgap lowering the operating wavelength. They are lattice-matched to GaAs substrate but very sensitive to the temperature. Visible VCSELs are also employed as optical data transmitter in polymer optical fiber (POF) network.

1.5   Success of VCSELs

VCSELs are not the only semiconductor lasers existing, they share the market with edge-emitting lasers (EELs). Nowadays, the only EELs survived on the market are the distributed feedback lasers (DFBs). Figure 1.5 shows a schematic EEL structure. The working principle of the two devices is practically the same: an active region providing gain sandwiched between two mirrors. Light is emitted in different directions: parallel to the wafer in EELs, perpendicular in VCSELs. The different plane of emission introduces several differences. EELs can reach higher power since the active region is longer with respect to VCSELs, where its length is determined by the epitaxial growth. Long active region, in turn, requires very low mirrors reflectivity to achieve lasing: huge DBRs are needed in VCSELs, whereas EELs can use simple cleaved facets as mirrors. On the contrary, the low volume of the active region in the VCSEL QWs makes the threshold current low minimizing the power dissipation. Furthermore, the circular geometry of VCSELs ensures a circular output beam with low divergence that can be directly coupled to the optical fiber. On the contrary, EELs produce an elliptical beam that needs a collimating lens system for optimal fiber coupling.

Another aspect that justifies the success of VCSELs is related to the production. VCSELs can be tested on wafer through a wafer probe setup: they don't need to be divided in single dies as EELs. The simple testing procedure, in turn, increases yield for manufacturers. Moreover, VCSEL-assembly uses the same mounting and packaging technology of light-emitting diodes (LEDs) reducing significantly the cost of the mass production. The small size, the geometry and the production of such devices make them suitable to be arranged in 1D or 2D arrays as Figure 1.6 shows.

This section is not intended to demonstrate the absolute superiority of VCSELs but to justify why these devices have captured a large market share.
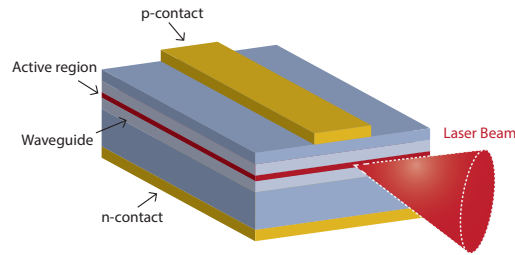
Figure 1.5.   Schematic EEL structure.
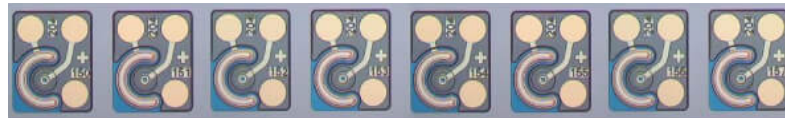
Figure 1.6.   1D VCSELs array.

1.6   VCSELs in optical links

In this section VCSELs performances are analysed from a telecommunication point of view.

The speed of transmission in multi-mode optical fibers (MMFs) for very-short distance (< 50 m) depends essentially on the transmitter modulation speed [8]. So, it is required a VCSEL with a high bandwidth regardless the number of lasing mode. Clearly, performance must be as much as possible temperature-independent. Several VCSELs working at 850 nm have been demonstrated to reach 50 Gbit/s [12, 13] with -3 dB electrical-to-optical (E-O) bandwidth as high as 30 GHz [12]. An improvement, while the laser is biased at low current density, has been registered by a coupled-cavity structure with multi-electrode device reaching 37 GHz E-O bandwidth [14]. Recently a novel device [8] operating at 940 nm has been demonstrated to reach a record-high -3 dB E-O bandwidths of 40 GHz (room temperature) and 32 GHz (85 °C). It allows to reach 60 Gbps over 1-m OM5 fiber under room temperature with a bit error rate (BER) less than 10^{-12}, without any signal processing.

In order to increase the bandwidth of the transmitter setup, it is possible to use more devices in parallel or to adopt special signal processing techniques. With the help of equalization for time domain interference elimination, an optical link has been demonstrated to reach 70 Gb/s non-return-to-zero (NRZ) transmission over 20 m OM4 MMF using a low cost device with a bandwidth of only 18 GHz [15]. Furthermore, high-level amplitude modulation formats can be adopted to increase the maximum data rate. In 2016, using digital signal processing (DSP) technique, 112 Gb/s PAM-4 transmissions over 100-m OM4 MMF have demonstrated at 850

nm [16]. In this work the attention will be paid more to the physical layer than to the system level. Indeed the whole transmission setup will be always improved starting from a better transmitter, with a higher bandwidth.

1.7 VCSELs market and future trends

The introduction of VCSELs as 3D-sensors in smartphones, starting with the image-recognition camera on Apple iPhone X, has given a huge boost to their market [17]. It is very probable that also Android phone producers will use VCSEL technology. A great demand from the market, billions of devices, needs a review of the manufacturing approach. VCSELs have always been a niche market: they are produced in small quantity on small wafer (100/150 mm) to have a reasonable yield. The requirement of more and more devices needs a mass-production that could be helped using bigger wafer; clearly the yield must remain reasonable. This latter is only an example to understand that not only the intrinsic device performance are the characteristic required from the next VCSELs generation: reproducibility and reliability must be taken into account. A good view of the market in the next years is given by Figure 1.7 that summarizes the results of a study on VCSEL industry, made by *Yole Développement*. After mobile market, the higher growth is the automotive area with two main applications. One is using VCSELs as in-cabin monitoring to track people in the car and the other is light-detection-and-ranging (LiDAR) [17] using larger VCSEL arrays due to high power requirement. This latter could be a good potential market but it is not so straightforward as stated by David Hall, principal marketing manager at National Instruments. *"There doesn't seem to be much overlap in requirements between a facial recognition system inexpensive enough to be integrated into a smartphone and a LiDAR system that's supposed to scan continuously much further than VCSELs could manage,"* Hall said. *"It remains to be seen if either one could benefit from the approach of the other."*
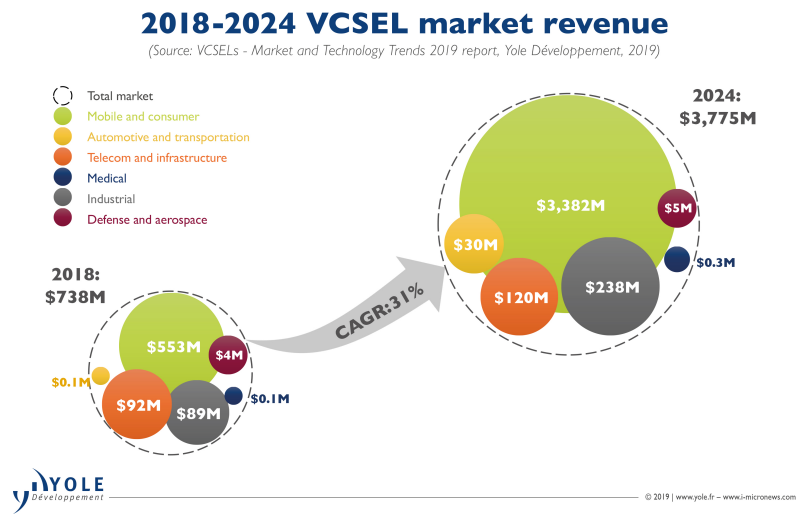
Figure 1.7.   VCSEL market revenue performed by *Yole Développement.*

Chapter 2

Model

The VCSEL structure described in Chapter 1 needs a very complex model. Different, strongly coupled, physical phenomena take place in the whole device and they determine its operation. A complete treatment would consider the solution of three main problems: electrical, thermal and optical. Clearly, a 3D simulation for all the variables of interest is required to have the best analysis. Many research groups have developed multiphysical VCSEL model like Politecnico di Torino with its multiphysical Vcsel Electro-opto-thermal NUmerical Simulator (VENUS) [18]. It includes a three-dimensional vectorial electromagnetic code, a description of the quantum well optical response, a heat equation solver, and a quantum-corrected drift-diffusion simulator. Due to its complexity and its precision, the model is time-consuming and unsuited for simulation of thousands of bits. Other models, less realistic, can be adopted to reduce simulation time like 1D drift-diffusion code D1ANA [19]. It is about 100 times faster than VENUS. It is of interest to have also simple and fast models for first-order analysis that at the same time obtain realistic simulation results. The rate equation model is one of the most common model used since its analytical solution is known.

2.1 Rate equation model

In this section, the simplest rate equation model is described and its analytical solution is derived. Simple analytical formulas are useful to understand better the effect of some parameters on the device operation. Rate equation model is simply described by two equations 2.1 and 2.2. The state variable, from which all the performance are extracted, are the carrier concentration N and the photon concentration N_p in the active region, the region where recombinations of electron and holes contribute to the photon emission. The spatial dependency is neglected: a constant concentration in the whole active region is assumed. It is important to

underline that the temperature-dependence is neglected.

$$\frac{dN}{dt} = \frac{\eta_i I}{qV} - (\frac{N}{\tau_c} + BN^2 + CN^3) - v_g g(N)N_p \tag{2.1}$$

$$\frac{dN_p}{dt} = \Gamma \beta_{sp} BN^2 - \frac{N_p}{\tau_p} + \Gamma v_g g(N)N_p \tag{2.2}$$

Equation 2.1, modelling the temporal evolution of the carrier density in the active region, can be simplified as

$$\frac{dN}{dt} = G_{gen} - R_{rec} \tag{2.3}$$

where G_{gen} represents the rate of injected electrons and R_{rec} the rate of recombining electrons per unit of volume. The first term is

$$G_{gen} = \frac{\eta_i I}{qV} \tag{2.4}$$

where η_i is the injection efficiency, the effective fraction of current that generates carriers in the active region, I is the input current, q is the elementary charge and V is the volume of the active region.

The recombination term includes different effects, related to the non-radiative, radiative, Auger recombinations and to the stimulated emission of photons.

$$R_{rec} = R_{nr} + R_{sp} + R_{Aug} + R_{st} = \frac{N}{\tau_c} + BN^2 + CN^3 + v_g g N_p \tag{2.5}$$

Carrier lifetime τ_c addresses impurity recombinations (Shockley-Read-Hall recombination), B accounts for the spontaneous emission of photons, over the whole bandwidth, while C takes into account non-radiative Auger contribution. The recombination leading to the emission of photons is modelled as the product of the group velocity v_g, the optical gain g and the photon density N_p. This latter term represents the coupling between equation 2.1 and 2.2.

The temporal evolution of the photon density N_p at the lasing wavelength in the active region is described by equation 2.2. Photon lifetime τ_p accounts for net-losses, the spontaneous emission factor β represents the fraction of the photons spontaneous-emitted having the same wavelength of the lasing mode and a direction compatible with the field propagation. The confinement factor Γ represents the ratio between the volume occupied by carriers and the volume occupied by photons. It is evaluated as

$$\Gamma = \frac{\int_{QW_s} n(z)|E(z)|^2 dz}{\int_L n(z)|E(z)|^2 dz} \tag{2.6}$$

where the numerator is an integral on the thickness of the QWs, the denominator is an integral on the whole length of the device, n is the refractive index and E is the electric field.

2.1.1 Static analysis

At threshold ($I = I_{th}$), stimulated emission can be neglected ($R_{st} = 0$). In steady state condition, forcing $\dfrac{dN}{dt} = 0$, equation 2.1 becomes

$$\frac{\eta_i I_{th}}{qV} = \frac{N_{th}}{\tau_c} + BN_{th}^2 + CN_{th}^3 \tag{2.7}$$

Above threshold, gain is equal to losses and a current increase results in an increase of the emitted photons. The carrier density is clamped to the value N_{th}. Therefore, above threshold, forcing a constant carrier density, equation 2.1 becomes

$$\frac{dN}{dt} = \frac{\eta_i(I - I_{th})}{qV} - v_g g(N_{th})N_p \tag{2.8}$$

Setting to zero the time derivate of the carrier density, a steady-state photon density

$$N_p = \frac{\eta_i(I - I_{th})}{qv_g g_{th}V} \tag{2.9}$$

is obtained, where $g_{th} = g(N_{th})$. The total optical energy stored in the cavity is

$$E_{OS} = h\nu N_p V_p \tag{2.10}$$

where ν is the central frequency and h is the Planck constant. The output optical power can be written as

$$P_{out} = \eta_O \frac{E_{OS}}{\tau_p} = \eta_O h\nu \frac{N_p V_p}{\tau_p} \tag{2.11}$$

where η_O is the optical efficiency defining the fraction of power that is output from the laser and E_{OS}/τ_p is the energy loss rate. Equation 2.11 can be simplified as

$$P_{out} = \eta_O \eta_i \frac{h\nu}{q}(I - I_{th}) \qquad (I > I_{th}) \tag{2.12}$$

Once the threshold is fixed by the losses, output power is linear with respect to the current for every bias above threshold. Such behaviour is not respected in a real device where temperature causes a droop in the power fo high bias as Figure 2.1 shows.
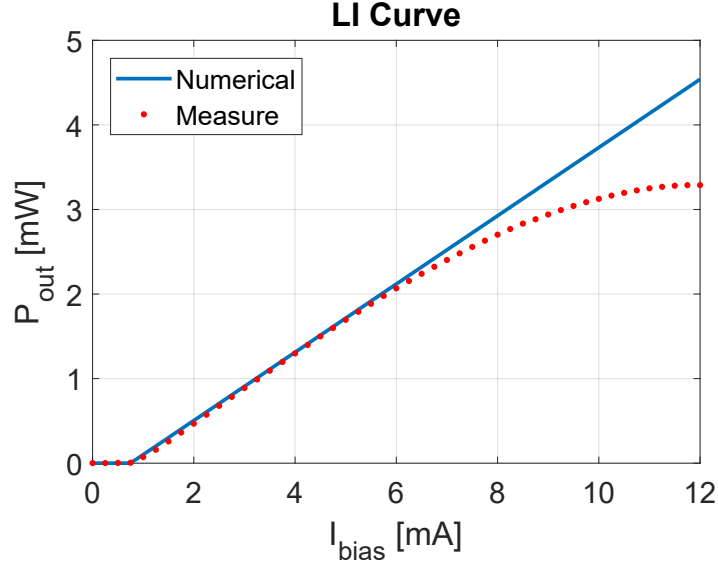
Figure 2.1. LI curve without temperature-dependence (blue curve) and experimental result with heating effect (red curve).

2.1.2 Dynamic analysis

In view of obtaining dynamic figure of merit such the -3dB bandwidth, a small signal analysis is performed. In the static characterization gain is considered a function only of the carrier density since the dependence on the photon density is not so relevant. On the contrary, it has a huge impact on dynamic analysis. For this reason, in this section, $g = g(N, N_p)$.

A small signal analysis starts exciting the laser with a small sinusoidal current with pulsation ω applied on an above-threshold DC current I_0

$$I(t) = I_0 + \delta I \sin(\omega t) \tag{2.13}$$

Since $\delta I \ll I_0$, suppose to work in linearity and assume

$$N(t) = N_0 + \delta N \sin(\omega t) \tag{2.14}$$
$$N_p(t) = N_{p0} + \delta N_p \sin(\omega t) \tag{2.15}$$

Linearising equation 2.1 and 2.2 around (N_0, N_{p0}) and defining

12

$$\tau_{\Delta N} = (\frac{1}{\tau_c} + 2BN_0 + 3CN_0^2)^{-1}$$
$$\tau'_{\Delta N} = (2\beta_{sp}BN_0)^{-1}$$
$$\gamma_{PN} = \frac{\Gamma}{\tau'_{\Delta N}} + \Gamma v_g a N_{p0}$$
$$\gamma_{PP} = \Gamma^2 \beta_{sp} B N_0^2 + \Gamma v_g a_p N_{p0}$$

where

$$a = \frac{\partial g}{\partial N}\Big|_{(N_0, N_{p0})}$$
$$a_p = \frac{\partial g}{\partial N_p}\Big|_{(N_0, N_{p0})}$$

after some calculations, it is obtained

$$\frac{\delta N_p}{\delta I} = \frac{\eta_i}{qV} \frac{\gamma_{PN}}{\omega_R^2} H(\omega) \tag{2.16}$$

$$\frac{\delta N}{\delta I} = \frac{\eta_i}{qV} \frac{\gamma_{PP} + j\omega}{\omega_R^2} H(\omega) \tag{2.17}$$

with the modulation transfer function

$$H(\omega) = \frac{\omega_R^2}{\omega_R^2 - \omega^2 + j\omega\gamma} \tag{2.18}$$

where ω_R is the resonance pulsation defined as

$$\omega_R^2 = \frac{v_g a N_{p0}}{\tau_p} + \left(\frac{\Gamma v_g a_p N_{p0}}{\tau_{\Delta N}} + \frac{\Gamma^2 \beta_{sp} B N_0^2}{N_{p0} \tau_{\Delta N}} \right) \left(1 - \frac{\tau_{\Delta N}}{\tau'_{\Delta N}} \right) + \frac{1}{\tau'_{\Delta N} \tau_p} \tag{2.19}$$

and γ is the damping factor defined as

$$\gamma = v_g a N_{p0} \left(1 + \frac{\Gamma a_p}{a} \right) + \frac{1}{\tau_{\Delta N}} + \frac{\Gamma^2 \beta_{sp} B N_0^2}{N_{p0}} \tag{2.20}$$

The modulation capability of a VCSEL is defined by equation 2.16. It expresses the variation of the photon density, which is proportional to the output power, with respect to the input modulated current. Therefore, $H(\omega)$ summarizes VCSEL

dynamical characteristics. The intrinsic small signal transfer function is that of a second order low-pass filter. Above threshold, equation 2.19 can be simplified as

$$\omega_R^2 \approx \frac{v_g a N_{p0}}{\tau_p} \tag{2.21}$$

This new definition helps to rewrite the damping factor as a function of the relaxation frequency $f_R = \omega_R/(2\pi)$

$$\gamma = K f_R^2 + \gamma_0 \tag{2.22}$$

where

$$K = 4\pi^2 \tau_p \left(1 + \frac{\Gamma a_p}{a}\right) \qquad \gamma_0 = \frac{1}{\tau_{\Delta N}} + \frac{\Gamma^2 \beta_{sp} B N_0^2}{N_{p0}} \tag{2.23}$$

The relaxation frequency increases with N_p: moving to higher bias current the bandwidth increases. Damping factor γ increases with the photon density as well. Therefore, the modulation bandwidth increases linearly with ω_R until damping becomes strong. A huge γ compromises the bandwidth that can be reduced. It exists an optimal value of the photon density, corresponding to the flattest modulation response, that maximize the - 3dB bandwidth. The maximum -3dB intrinsic bandwidth can be derived from the K-factor, defined in equation 2.23, as

$$f_{3dBmax} = \sqrt{2}\frac{2\pi}{K} \tag{2.24}$$

An example of the transfer function $H(\omega)$ is shown in Figure 2.2. It has been evaluated for different relaxation frequencies and the corresponding damping factor is calculated forcing $K = 0.3$ ns, a reasonable value for a commercial laser. Figure shows clearly that for high value of f_R (purple curve) the bandwidth stop to be increased: the huge damping factor (750 ns) reduces it. The optimal value of the -3dB bandwidth is represented by the flattest modulation response (yellow curve).

2.2 Temperature-dependent rate equation model

Temperature affects significantly VCSELs performances. A thermal characterization is useful to have consistent simulated results. The model subsequently analysed follows this aim. It is a rate equation model, temperature-dependent, described simply by equations 2.25, 2.26 and 2.27. The first two represent the same equation 2.1 and 2.2 with the introduction of the temperature. The spatial dependency is always neglected: a constant concentration in the whole active region is assumed. The temperature is described by equation 2.27. It is evaluated as the product between
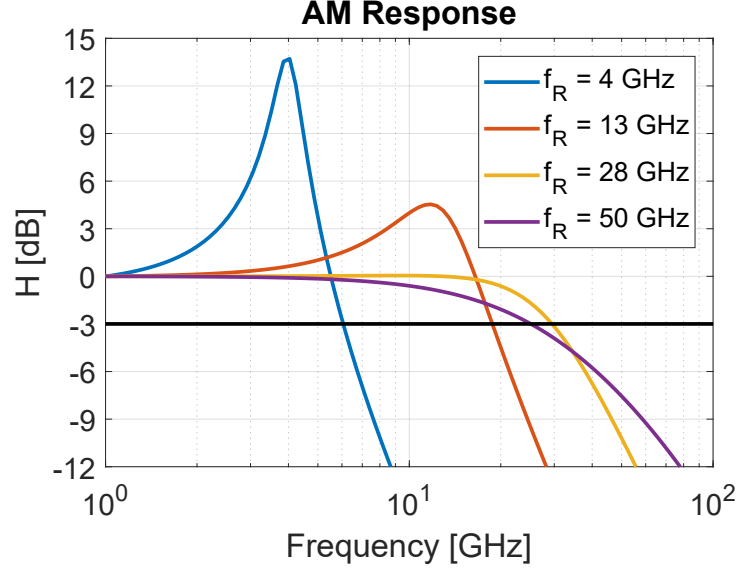
Figure 2.2.   Intrinsic modulation transfer function for different relaxation frequencies with $K = 0.3$ ns. The corresponding damping factors are 4.8 (blue), 51 (red), 235 (yellow) and 750 (purple) ns.

dissipated power and a thermal resistance R_t. Dissipated power is simply the difference between input electrical power (current I times voltage V) and output power P. Since the model described is not able to generate the voltage-to-current (VI) characteristic, V is considered an input and must be taken from measurements. Temperature is not treated dynamically since thermal time constants are at least 1000 times slower than all of the ones involved in VCSEL simulation [20]. It is of interest to underline that the gain is a function of the wavelength λ. Its shift can be evaluated starting from the temperature rise.

$$\frac{dN}{dt} = \frac{\eta_i I}{qV} - (\frac{N}{\tau_c} + R_{sp}(N,T) + C(T)N^3) - v_g g(N, N_p, T, \lambda)N_p \qquad (2.25)$$

$$\frac{dN_p}{dt} = \Gamma\beta_{sp}R_{sp}(N,T) - \frac{N_p}{\tau_p(T)} + \Gamma v_g g(N, N_p, T, \lambda)N_p \qquad (2.26)$$

$$T = R_t(I \cdot V - P) \qquad (2.27)$$

Next sections will explain in detail the model used for some physical quantity present in the rate equation model.

2.3 Active region model

Active region strongly determines the operation of the device; particularly the semiconductor alloy used as active material defines the optical response of VCSELs. Therefore, a precise model is useful to have a correct characterization of the optical response of the active semiconductor as a function of temperature and wavelength. The main ingredients that must be modelled are gain, spontaneous emission, Auger coefficient and volume of the active region.

2.3.1 Gain

The model used for gain is a three-parameter logarithmic model commonly adopted in laser modelling:

$$g(N, N_p, T, \lambda) = \frac{g_0(T, \lambda) \cdot \log(\dfrac{N}{N_{tr}(T, \lambda)})}{1 + \epsilon N_p} \tag{2.28}$$

where g_0 is an empirical gain coefficient, N_{tr} is the transparency carrier density, i.e. $g(N_{tr}) = 0$, and ϵ is the gain compression factor describing non-linear dependency of the material gain on N_p, caused by spectral holeburning and carrier heating effects. In this model, only the first two parameters depend on temperature and wavelength. In view of extracting g_0 and N_{tr} some reference curves are needed. Since gain measurements are not available and, in general, they are not so easy to be performed, reference curves are evaluated with a more sophisticated solver. It requires the computation of the band structure of the QW active region. A 4-band $k \cdot p$ method has been used, including electrons, heavy holes, light holes and the split-off band. An eigenvalue problem is solved for each transverse electron wavevector k in order to obtain the QW subbands. The optical gain g is obtained from the imaginary part of the carrier-induced permittivity change $\Delta\epsilon_{QW}$ of a QW. This latter can be computed by Fermi's golden rule as the sum of all of its electron/hole subbands l,m

$$\Delta\epsilon_{QW}(n, p, \lambda, T) = \sum_{l,m,\mathbf{k}} |\hat{\mathbf{e}} \cdot \mathbf{M}_{l,m}(\mathbf{k})|^2 (f_{c,l} - f_{v,l}) \mathcal{L}(\Delta E) \tag{2.29}$$

where $\mathbf{k}$ is the wavevector, $\mathbf{M}_{l,m}(\mathbf{k})$ is the transition dipole matrix that can be evaluated from the overlap of the eigenfunctions resulting from the computation of the band structure, and $\Delta E = E_{l,m}(\mathbf{k} - h\omega)$ [18]. An example of the gain spectra of InGaAs QW is shown in Figure 2.3.

The routine saves gain in a 3-D (electron density, wavelength and temperature) look-up table (LUT) that will be interpolated during the simulation of the rate equation model to extract g_0 and N_{tr}. It is of interest to analyse in details the extraction of the parameters characterizing the gain whose flowchart is summarized in
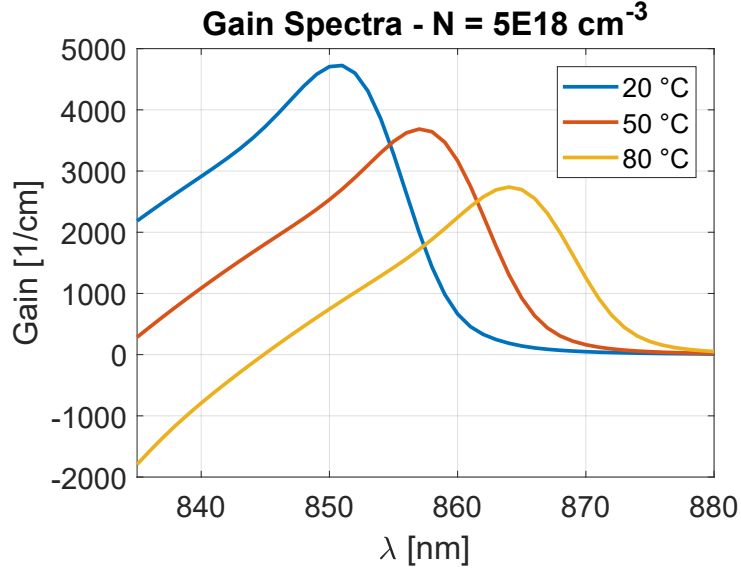
Figure 2.3. InGaAs gain spectra for different temperatures and a fixed carrier density $N = 5\text{E}18\ cm^{-3}$. Blue, red and yellow refer to 20, 50 and 80 °C.

Figure 2.4, left. The first step is to pass from a 3-D LUT to a 1-D one that depends only on carrier density. It is possible to do it by means a spline interpolation at a fixed wavelength and temperature. After the interpolation, a vector containing all the values of gain at the query carrier density points is ready to be fitted with 2.28. During the simulation, the fitting with respect to the reference gain curves is performed in a small range of carrier density near the threshold forcing $\epsilon = 0$. The two parameters g_0 and N_{tr} are analytically evaluated with two simple formulas (2.30). They represents the analytical solution of a 2×2 system derived by imposing the passage of the logarithmic curve through two points (N_A, g_A) and (N_B, g_B) of the reference curve.

$$
\begin{cases}
g_0 = \dfrac{g_B - g_A}{\log\left(\dfrac{N_B}{N_A}\right)} \\[4mm]
N_{tr} = N_B \exp\left(-\dfrac{g_B}{g_0}\right)
\end{cases}
\tag{2.30}
$$

An example of gain fit is shown in Figure 2.5, left. The range of carrier density on which the fit is performed is very large to demonstrate the strengths and the weaknesses of the model. A good fit is lost when the gain curves do not follow a logarithmic behaviour as the curve for 20 °C suggests. Generally, it happens for very low threshold carrier density. A more realistic scenario, above threshold, is represented in 2.5, right. Now, fit for 20 °C is no more a problem since the range of
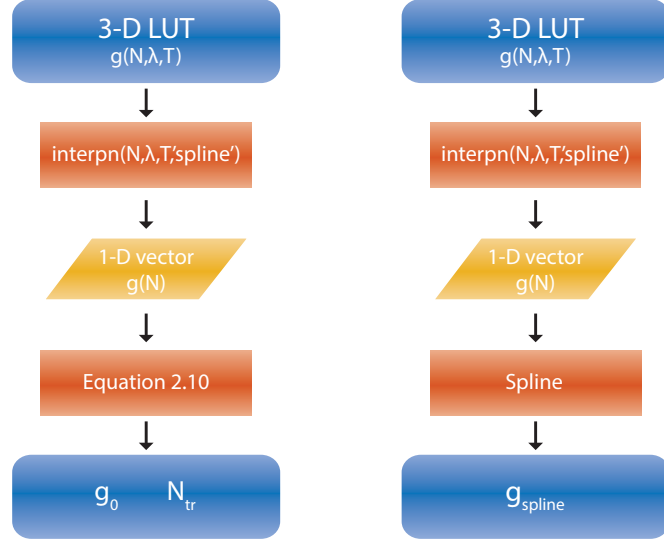
Figure 2.4. Left: Flowchart of the extraction of g_0 and N_{tr} using logarithmic fit. Right: Flowchart of the extraction of the 1-D spline.

interest is significantly reduced. During the simulation, the range of carrier density is very small since, above threshold, N is fairly constant. Moreover, $g0$ and N_{tr} are updated at each bias points; above threshold, the bias mesh can be done dense enough that the variation of carrier density, from one bias point to the other one, can be reduced significantly enhancing the quality of the fit. As seen, logarithmic model can fall in a specific range of carrier density, where the gain changes curvature. In order to test its validity and verify its speed, logarithmic model is compared with a very precise but more time-consuming gain model, based on a cubic 'spline' interpolation. Its flowchart is represented in Figure 2.4, right. In mathematics, a cubic spline is a special function defined piecewise by third-order polynomials. A cubic polynomial is defined by four coefficients. Given a number of interpolating points n, at each interior knot four constrains are needed to define each polynomial giving $4n$ coefficients in total. Both polynomials that meet at the same interpolating point must take the same value, the same first and second derivative. At the end, parametrizing polynomials, a tridiagonal system of size $\propto n$ must be solved. Therefore, it requires much more time with respect the logarithmic fit previously analysed that uses two analytical formulas. Figure 2.6 shows a comparison between cubic spline and logarithmic fit for a specific temperature and wavelength where gain has a change of curvature with $g_{th} = 590cm^{-1}$. As stated before, reducing the range of carrier density both models match. See Chapter 3 for a qualitative comparison of both models in the simulation.

18
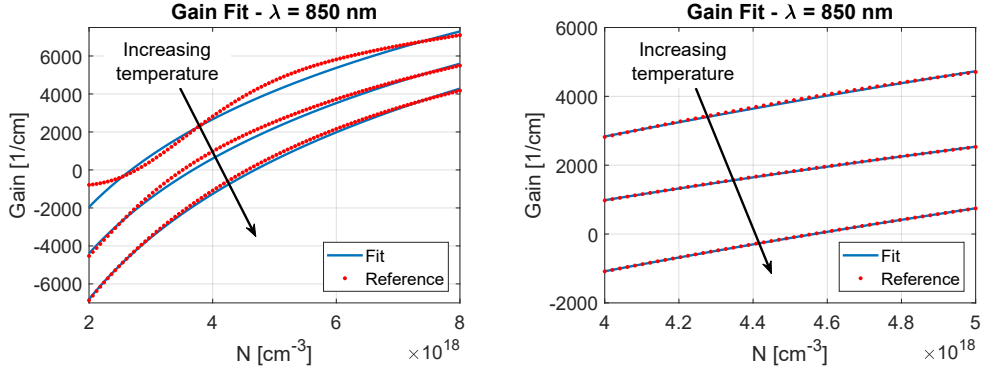
Figure 2.5. Left: gain fit for T = [20,50,80] °C at $\lambda = 850$ nm. Right: a refine fit in a small range of carrier density.
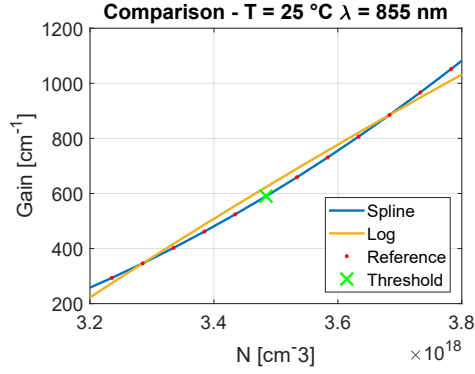
Figure 2.6. Spline (blue) and logarithmic (yellow) fit comparison. Green cross evidences the point defining threshold gain and threshold carrier density.

2.3.2 Spontaneous emission

A common model adopted to represent the total spontaneous emission R_{sp} as a function of the carrier density is a quadratic model. Generally the linear term is neglected but, in this work, it is taken into account to achieve a better fit:

$$R_{sp}(N,T) = B_q(T)N^2 + B_l(T)N \qquad (2.31)$$

The same QWs optical solver used to create the gain reference curve is able to provide also the total spontaneous emission. It is saved in a 2-D LUT (temperature and carrier density); B_q and B_l are extracted with the same gain algorithm. Clearly, the equation to evaluate B_q and B_l are different since here is a quadratic model

19

and not a logarithmic one. The solution of the 2×2 system gives

$$\begin{cases} B_q = \dfrac{1}{(N_B - N_A)} \left(\dfrac{R_{sp_B}}{N_B} - \dfrac{R_{sp_A}}{N_A} \right) \\ B_l = \dfrac{R_{sp_A}}{N_A} - N_B B_q \end{cases} \tag{2.32}$$

where (N_A, R_{sp_A}) and (N_B, R_{sp_B}) are the interpolating points of the reference curve.

An example of InGaAs fit is represented in Figure 2.7.
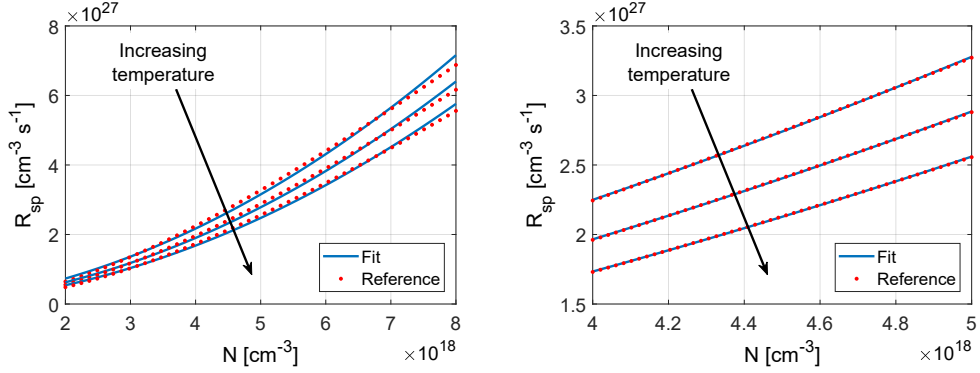
Figure 2.7.   Left: total spontaneous emission fit for T = [20,50,80] °C. Right: a refine fit in a small range of carrier density.

2.3.3   Volume

The shape of the active region defines the carriers volume. It is evaluated as

$$V = F N_{QW} d_{QW} \pi r^2 \tag{2.33}$$

where F is a fitting parameters, N_{QW} is the number of QWs, d_{QW} is the height of a single QW and r is the radius of the oxide aperture. The transverse area in which the carriers are confined is unknown: the model uses an equivalent area defined by the circular oxide aperture multiplied times F. This latter is set to match dynamic measurements. See Chapter 3.

2.3.4   Auger recombination

Auger recombination may play a crucial role at high carrier/current density, leading to current droop in VCSEL. For this reason, a model to characterize its behaviour

versus the temperature is needed. The model used in this work

$$C(T) = C_0 \exp\left(\frac{T - T_0}{100K}\right) \qquad (2.34)$$

follows an exponential behaviour [21]. T_0 is the stage temperature and C_0 is the corresponding Auger recombination factor.

2.4 Thermal roll-over model

In order to understand how to model the thermal droop, let us recall the analytical equation 2.12. Power can be lowered playing on the threshold current I_{th} or on the differential efficiency (the product of η_O and η_i) . Threshold current is affected by the gain model previously analysed. Indeed, temperature and wavelength variations change the shape of the active material gain since g_0 and N_{tr} depends on them. As a consequence the threshold gain g_{th} changes the corresponding threshold carrier density N_{th}, and I_{th} in turn varies with temperature and wavelength. The effect induced by the gain-model is not able to lower significantly the power in the devices analysed. So, the idea is to try to increase g_{th} enhancing phenomenologically the optical losses. They can be increased lowering the photon lifetime τ_p. On the other hand, it is also possible to play on another parameter, the injection efficiency. It acts both on the power-current slope and on I_{th}. Next sections introduce the modelling of η_i and τ_p analysing their effect on light-to-current (LI) curve. It is key to understand which of the two parameters affect more the device operation.

2.4.1 Photon lifetime

The first attempt is made varying photon lifetime. It is determined by the modal losses in the cavity. Higher temperatures enhance losses, leading to a reduction of the photon lifetime. The model adopted assumes the following empirical dependence

$$\tau_p(T) = \frac{\tau_{p0}}{\dfrac{T - T_0}{T_{\tau p}} + 1} \qquad (2.35)$$

where τ_{p0} is the photon lifetime at a temperature T_0 whereas $T_{\tau p}$ represents the temperature above T_0 at which the photon lifetime is halved. A parametric analysis for different $T_{\tau p}$.

2.4.2 Injection efficiency

Injection efficiency accounts for lateral leakage currents and carrier overflow over confining barrier. Temperature affects the fraction of current that recombines in
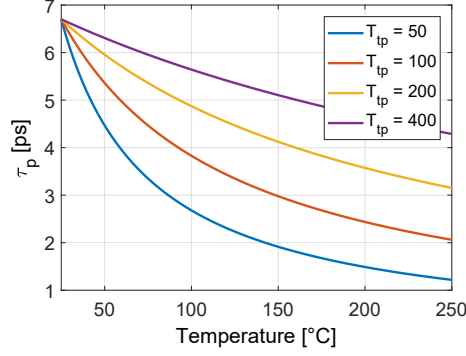
Figure 2.8. Photon lifetime as a function of temperature for various values of $T_{\tau p}$ with $\tau_{p_0} = 6.7$ ps at $T_0 = 25$ °C.

the QWs so that $\eta_i(T)$ has a crucial role to model the dependences on temperature in lasers [22]. The model adopted for the injection efficiency (2.36) follows a Fermi function behaviour. Such function maintains a fairly constant behaviour for low temperatures and a decreasing behaviour for higher temperatures. Furthermore, its value is between 0 and 1.

$$\eta_i(T) = \frac{\eta_{i0}}{1 + \exp\left(\dfrac{T - T_\eta}{T_{th}}\right)} \tag{2.36}$$

The value of the efficiency at low temperature is dictated by η_{i0}, T_η represents the temperature at which the injection efficiency is halved whereas T_{th} controls the shape of the Fermi function. The effect of the last two parameters is shown in 2.9.
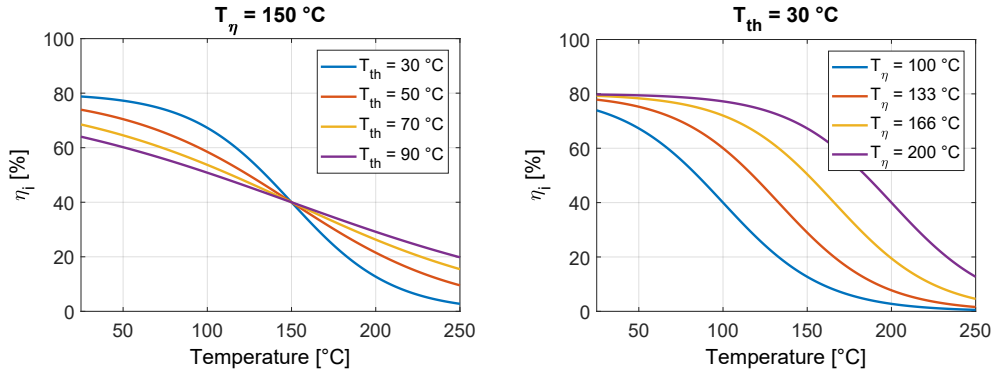

Figure 2.9. Left: injection efficiency for various T_{th} with $T_\eta = 150$ °C and $\eta_{i0} = 0.8$. Right: injection efficiency for various T_η with $T_{th} = 30$ °C and $\eta_{i0} = 0.8$.

2.4.3 Injection efficiency VS photon lifetime

In order to understand the effect of both parameters on the LI curve a parametric analysis is performed compared with measured results. Figure 2.10 shows the effect of the injection efficiency when the photon lifetime is set constant versus temperature ($T_{\tau p} = \infty$) while Figures 2.11 and 2.12 does the opposite ($T_\eta = \infty$). A good match is obtained just considering internal efficiency droop. Photon lifetime should change a lot (from ≈ 5 ps to less than 1 ps) in order to have a good match. The corresponding threshold gain in 2.12, right, is dramatically varying like the carrier density behaviour in Figure 2.11, right. The photon lifetime effect seems to be too strong. As a consequence, the model uses only η_i as the main ingredient to cause thermal roll-over. It would be of interest to have some measurements of η_i and τ_p in view of verifying the correctness of such phenomenological approach.
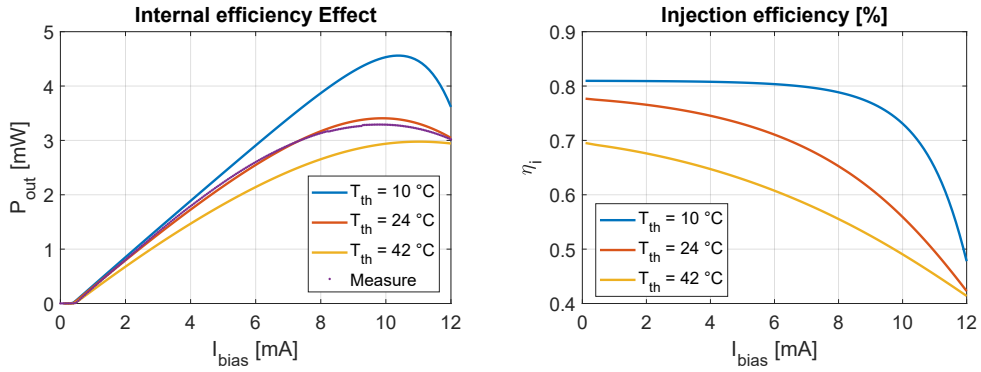

Figure 2.10. Left: LI curves for various T_{th} with $T_{\tau p} = \infty$ and $T_\eta = 93$ °C. Right: the corresponding η_i for various T_{th} with $T_\eta = 93$ °C.
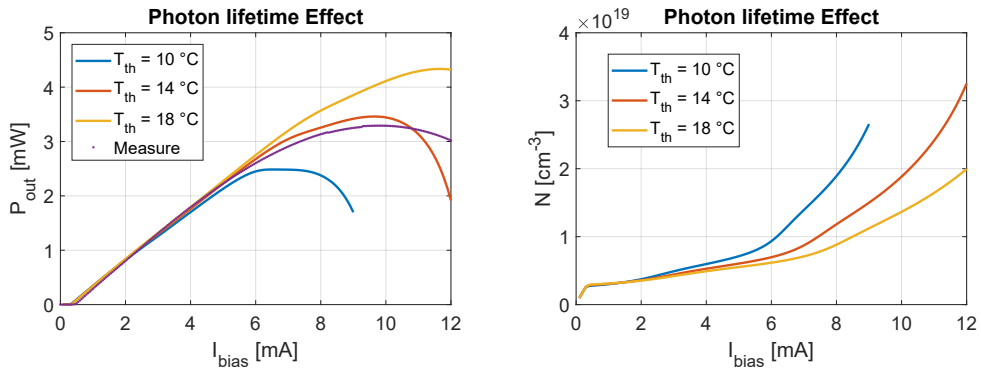

Figure 2.11. Left: LI curves for various T_{tp} with $T_\eta = \infty$. Right: the corresponding carrier density for various T_{tp} with $T_\eta = \infty$.
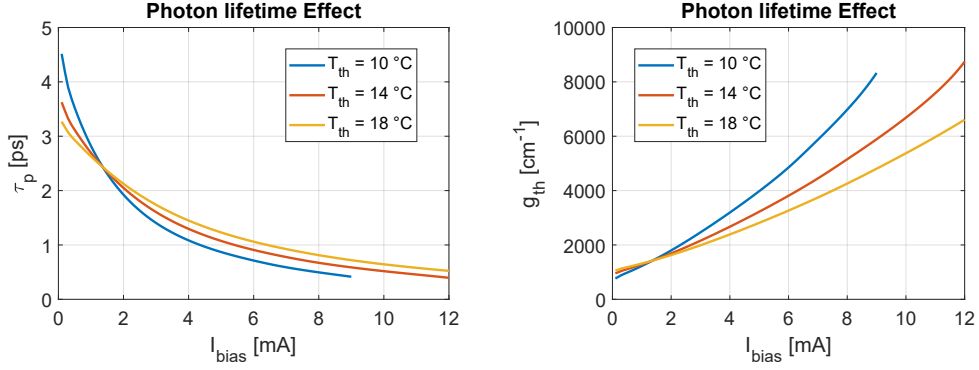
Figure 2.12. Left: photon lifetime for various T_{tp} with $T_{1/2} = \infty$. Right: the corresponding threshold gain for various T_{tp} with $T_{1/2} = \infty$.

2.5 Temperature-dependent steady-state solution

The behaviour of a laser is well-described by its LI curve. It shows the amount of power emitted under a constant input current. The steady-state solution of the coupled equations 2.1 and 2.2 gives the LI curve. They are solved numerically using the Runge-Kutta 4th order method, which provides the temporal evolution of the carrier and photon density in the active region. A constant current over a given time window, sufficiently large to reach the steady-state, is set as input and the corresponding output power is evaluated from the steady-state photon density as

$$P_{out} = \eta_O h\nu \frac{N_p V}{\Gamma \tau_p} \tag{2.37}$$

where η_O is the optical efficiency, defining the percentage of the light coupled out, h is the Plank constant and ν is the VCSEL frequency.

The algorithm used to contruct the LI curve uses the following steps:

1. At the k-th step, rate equations are solved for a given bias point I_k at a temperature T_{k-1} and a wavelength λ_{k-1}.

2. Temperature at step k is evaluated as

$$T_k = R_{tk}(I_k \cdot V_k - P_k) \tag{2.38}$$

where R_{tk} is the thermal resistance, V_k is the voltage and P_k is the output power at the k-step.

3. Wavelength at step k is evaluated as

$$\lambda_k = \lambda_0 + \Delta\lambda(T_k - T_0) \tag{2.39}$$

where λ_0 and T_0 are, respectively, the initial wavelength and initial temperature and $\Delta\lambda$ is a coefficient that measures the wavelength shift due to temperature. For VCSEL in the range of 850 nm, the mode shift $\Delta\lambda \approx 0.07nm/K$ [23].

4. All parameters are updated with λ_k and T_k.

2.5.1 Runge-Kutta 4th order method

This section focuses on the briefly introduction of the numerical method used to solve the differential equation 2.1 and 2.2.

The Runge-Kutta 4th order method is an iterative numerical method used to find approximate solutions of ordinary differential equations (ODEs). Equations 2.1 and 2.2 are two 1st order ODEs and they can be generalized as follows

$$\begin{cases} \dfrac{dN}{dt} = f(N, N_p, t) \\ \dfrac{dN_p}{dt} = g(N, N_p, t) \end{cases} \tag{2.40}$$

Let a time interval $[t_0, t_f]$ be defined. It is divided in N subintervals whose size is $h > 0$. An uniform mesh is used so that

$$h = \frac{t_f - t_0}{N}$$

At the initial time t_0 the corresponding (N,N_p) values are (N_0,N_{p0}) and they are given. Starting from t_0 is possible to arrive to the final step t_f using the following formula for $i = [0,1,...,N]$

$$\begin{cases} N_{i+1} = N_i + \dfrac{1}{6}h(k_0 + 2k_1 + 2k_2 + k_3) \\ N_{p_{i+1}} = N_{p_i} + \dfrac{1}{6}h(l_0 + 2l_1 + 2l_2 + l_3) \end{cases} \tag{2.41}$$

where

$$
\begin{cases}
k_0 = f(N_i, N_{p_i}, t_i) \\[2mm]
l_0 = g(N_i, N_{p_i}, t_i) \\[2mm]
k_1 = f(N_i + \dfrac{1}{2}k_0, N_{p_i} + \dfrac{1}{2}l_0, t_i + \dfrac{1}{2}h) \\[2mm]
l_1 = g(N_i + \dfrac{1}{2}k_0, N_{p_i} + \dfrac{1}{2}l_0, t_i + \dfrac{1}{2}h) \\[2mm]
k_2 = f(N_i + \dfrac{1}{2}k_1, N_{p_i} + \dfrac{1}{2}l_1, t_i + \dfrac{1}{2}h) \\[2mm]
l_2 = g(N_i + \dfrac{1}{2}k_1, N_{p_i} + \dfrac{1}{2}l_1, t_i + \dfrac{1}{2}h) \\[2mm]
k_3 = f(N_i + k_2, N_{p_i} + l_2, t_i + h) \\[2mm]
l_3 = g(N_i + k_2, N_{p_i} + l_2, t_i + h)
\end{cases}
\tag{2.42}
$$

Looking only at the first equation of 2.41 (same considerations hold for the other), the solution at each point of the mesh N_{i+1} is approximated as the sum of previous values N_i and the average of 4 slopes:

- k_0 is the slope at the beginning of the subinterval $[t_i, t_{i+1}]$

- k_1 is the slope at the midpoint of the subinterval $[t_i, t_{i+1}]$ using k_0 as increment

- k_2 is the slope at the midpoint of the subinterval $[t_i, t_{i+1}]$ using k_1 as increment

- k_3 is the slope at the end of the subinterval $[t_i, t_{i+1}]$ using k_2 as increment

The previous explanation is clearer remembering that f is the time derivate of N and that g is the time derivative of N_p.

Fourth-order method means that the local truncation error is on the order of $(\mathbf{O}(h^5))$.

2.6 Temperature-dependent dynamic analysis

Dynamic behaviour summarizes the capability of a VCSEL to act as a transmitter; in fact, the bandwidth of the laser determines the maximum achievable modulation speed.

Small signal analysis is performed numerically to find the intrinsic E-O transfer function $H_{int}(w)$. As first step, steady-state solution is found for a given bias point I_0, defining all the initial state-variables at the correct temperature around

which the small perturbation is applied. Then, for each frequency point, rate equations are solved using as input a sinusoidal signal with small amplitude. The corresponding optical output, normalized on the input current, will define $H_{int}(w)$. The temperature variations, determined by the sinusoidal input, are not considered since they are small: thermal time constant are much slower than all the others involved in the simulations. For this reason, numerical solver is needed only for the static characterization since temperature changes only the initial conditions at I_0. Once they are fixed, the analytical solution of the small signal analysis is exactly the same of that explained in section 2.1.2. As expected, Figure 2.13 shows a perfect match between numerical (dotted curves) and analytical (solid lines) solution for all temperatures. The result obtained is very useful since analytical formulas require a very fast execution time and they can replace the numerical solver.
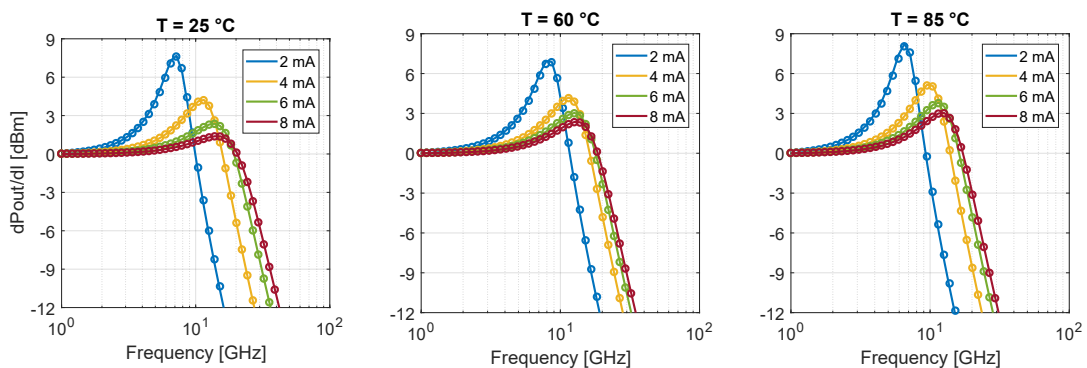

Figure 2.13. Analytical and numerical small signal analysis comparison for three different temperatures and four different currents. From left to right: 25, 60 and 85 °C. Circles refer to numerical simulated results whereas solid lines refer to the analytical solution. Blue, yellow, green and red refer, respectively, to 2, 4, 6 and 8 mA.

2.6.1 Parasitic response

The procedure illustrated in the previous section provides the intrinsic transfer function that is not the one measured from a real device. Indeed, the bandwidth of a VCSEL is affected by parasitics, especially when dealing with high-frequency. Therefore, it is necessary to introduce a model for the parasitics, whose effect is described by a transfer function H_{ext}.

The model adopted is shown in Figure 2.14. The VCSEL is described by four elements: C_p, R_m, C_m and R_j. Moreover, it is driven by a voltage source V_s with a characteristic impedance Z_0. The pad capacitance C_p represents the capacitance between the signal and the ground, R_m takes into account the mirrors and the

contact resistance, C_m is the sum of the oxide capacitance and the diode junction capacitance of the active region while R_j is the junction resistance.
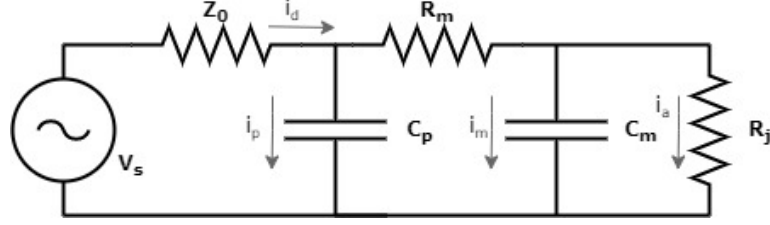

Figure 2.14.   Parasitic model.

Considering the circuit in Figure 2.14, the extrinsic transfer function is

$$H_{ext}(w) = \frac{i_a(w)}{V_s} = \frac{1}{a_0 + j\omega a_1 - \omega^2 a_2} \tag{2.43}$$

where

$$a_0 = Z_0 + R_j + R_m$$
$$a_1 = (R_m R_j C_j + Z_0(R_j(C_p + C_a) + C_p R_m))$$
$$a_2 = Z_0 C_p R_j C_j R_m$$

that is commonly approximated with a single-pole low-pass filter transfer function:

$$H_{ext}(w) = \frac{1}{1 + j\dfrac{\omega}{\omega_0}} \tag{2.44}$$

where ω_0 is the parasitic roll-off frequency, easy to use as fitting parameter when measurements of the parasitic are not available.

Finally, the overall frequency response $H(w)$ is

$$H(w) = H_{ext}(w) \cdot H_{int}(w) \tag{2.45}$$

The parasitics parameters C_p, R_m, C_m and R_j can be easily extracted from measurements de-embedding $S11$-parameter through a commercial RF tool. A schematic circuit, i.e. Figure 2.15, left, is given to the RF software. Using an optimization tool, it changes the four parameters in order to match the measurement. A result is shown in figure 2.15, right.
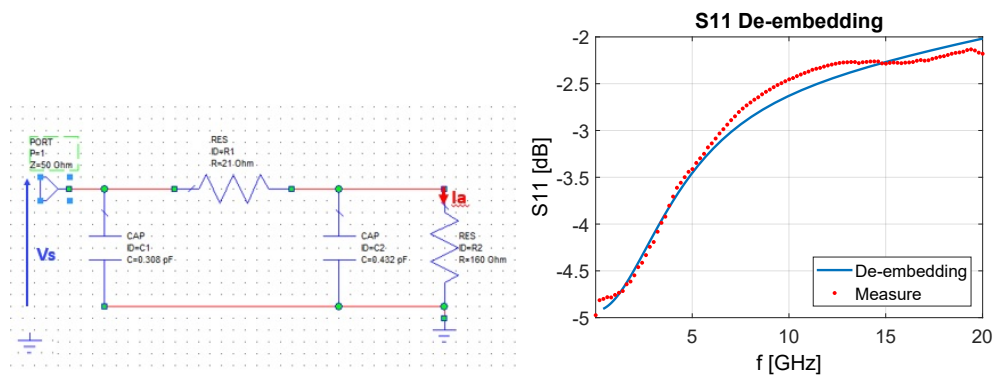
Figure 2.15.   Left: schematic circuit used for de-embedding. Right: a comparison between measurement and de-embedding result.

Chapter 3

Simulation

In Chapter 3 the temperature-dependent rate equation model is applied to a real VCSEL provided by industrial partner TRUMPF Photonics. The device is a 850 nm InGaAs-AlGaAs multimodal laser with a 7 μm oxide aperture.

3.1 Active region

The first task to perform a simulation is to identify the correct type of semiconductor alloy and the shape of the QWs used for the active region in order to extract the gain and spontaneous emission curves. More precisely, in this case, it is necessary to fix the width of the QWs and the percentage of Indium. These are the two main ingredients used to create gain reference curves. The width of the QWs is fixed by the nominal value declared by TRUMPF while the percentage of Indium (%4.8) is changed in order to match the photoluminescence (PL) measurement. TRUMPF declared a peak of the PL at 837.5 nm at room temperature. PL is performed as follows. A beam of photons is focused on the semiconductor. If the energy of photons coming from the source is greater than the energy gap of the semiconductor, the sample emits photons. These are collected and analysed. PL can be considered directly proportional to the spontaneous emission spectrum at low carrier density. Figure 3.1 shows the matching between the PL measurement and the active region spontaneous emission spectrum at low pumping evaluated by the VENUS routine.

3.2 LI Curve

As first step, static characterization is performed. The list of parameters used in the simulation is summarized in Table 3.1. Starting from 0 mA to 12 mA with a non-uniform mesh, more dense near threshold, a step of current for each bias point is applied until the steady-state value is reached. Figure 3.2 shows an example of the time evolution of carrier density, photon density and gain in the active region
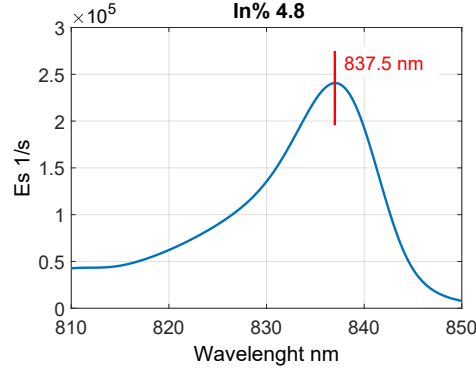
Figure 3.1. Spontaneous emission spectrum at low carrier density at room temperature with 4.8% of Indium.

when a step current of 6 mA is applied. This figure explains in a clear manner the behaviour of a laser. When the carrier density is lower than the threshold value, gain is negative and the corresponding photon density is very low, only dominated by spontaneous emission. An increase of carrier density is required to have positive gain inducing so stimulated emission. N must increase so that gain compensates losses: device starts lasing.

Parameters	Value	Unit
η_{i0}	0.8	•
T_{th}	28	K
$T_{1/2}$	437	K
η_O	0.43	•
τ_c	2.2	ns
λ_0	848.5	nm
$\Delta\lambda$	0.067	nm/K
T_0	298	K
R_t	2666	K/W
Γ	0.028	•
ϵ	2E-17	cm^3
τ_{p_0}	6.7	ps
T_{τ_p}	∞	•
V	1.1E-12	cm^3
v_g	9.08E7	m/s
β	0.01	•
C_0	5E-31	cm^6/s

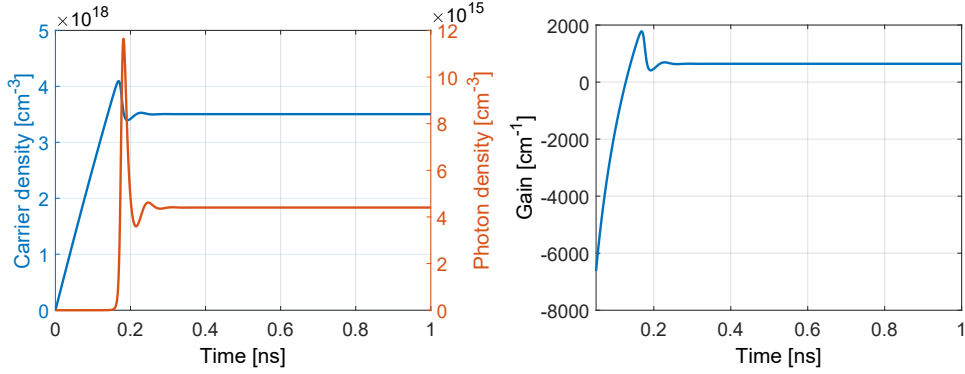Table 3.1. List of parameters used in the simulations.

Figure 3.2. Left: time evolution of carrier (blue) and photon (red) density with a current of 6 mA. Right: the corresponding gain evolution.

Steady-state values of carrier and photon density are used to construct LI curve for different temperatures shown in Figure 3.3. The parameters are fitted at 25 °C; for all other temperature they are evaluated with equations discussed in Chapter 2. Figure 3.4, left, shows a LI curve zoom near threshold (coloured curves) compared with the interpolation of the first two measured powers above threshold (black curves). Interpolation is useful to extract correctly the value of the threshold current. As figure shows, a good match in the threshold is obtained only for 25 °C (blue curve) where η_{i0} and τ_c are tuned. For 60 (red) and 85 °C (green), threshold is much higher with respect to the measured results. No parameters can be changed to reduce the high threshold since all the parameters at low bias are very close to the value at 25 °C and they can only be degraded. To evaluate the responsible of such high threshold, an investigation on the gain can be performed since it fixes the threshold carrier/current density and it is a function of temperature and wavelength. It is important to underline that temperature and wavelength shifts match the measured results as Figure 3.5 justifies. It is expected since R_t and $\Delta\lambda$ are evaluated from measurements; only a little bit of tuning on λ_0 is performed. As a consequence, only the gain shape can be the responsible of such high threshold. Figure 3.4, right, evidences the big variation of the threshold carrier density N_{th}, taken from the gain-LUT evaluated at threshold. N_{th} is the carrier density at which the three coloured curves intersect the threshold modal gain (black curve). Blue curve refers to 25 °C and $\lambda = 848.5$ nm, red curve refers to 60 °C and $\lambda = 851.5$ nm and green curve refers to 85 °C and $\lambda = 852.5$ nm. The equally spaced N_{th}, induced by the gain, are the responsible of the equally spaced threshold currents. As expected, N_{th} variation matches the corresponding values taken from the simulation as Figure 3.6, left, demonstrates. At the end, it seems that the gain has not been evaluated in the correct wavelength range where InGaAs shows a temperature-independent behaviour. A new parameter dλ can be introduced to achieve a better matching. See next section.
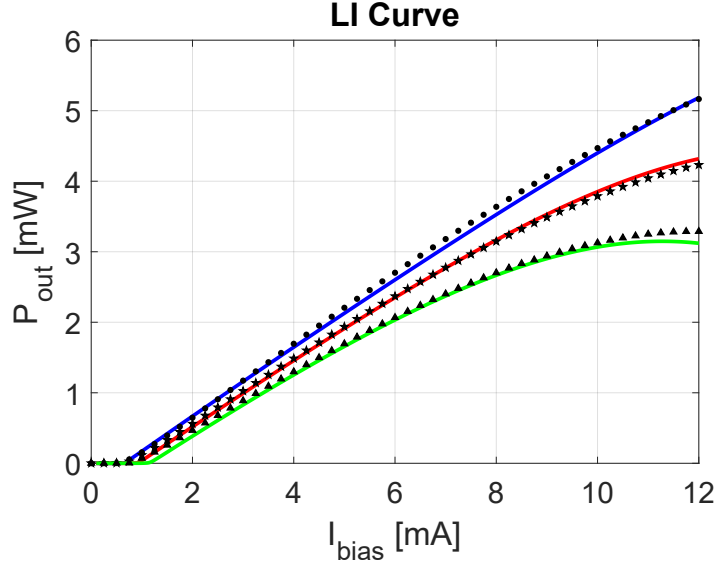
Figure 3.3. LI curves for different temperatures near threshold. Coloured solid lines encode numerical results. Blue, red and green refer respectively to 25, 60 and 85 °C. Black symbols encode measured data. Circle, star and triangle refer respectively to 25, 60 and 85 °C. Solid black lines are interpolating curves passing through the first two symbols above threshold.
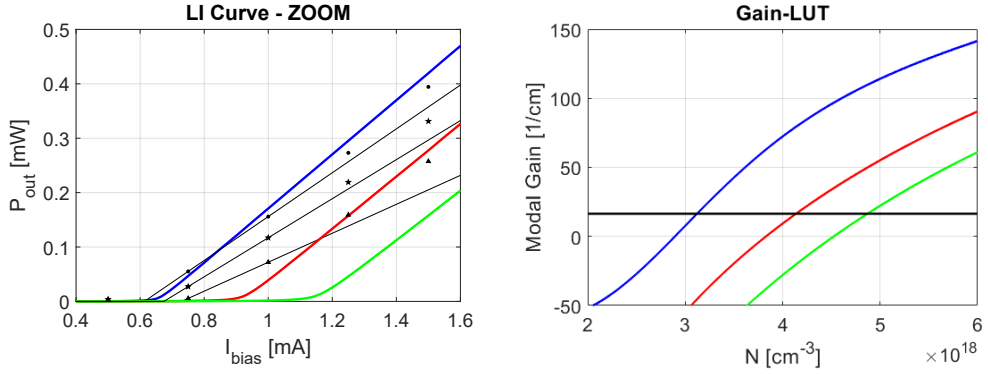
Figure 3.4. Left: LI curves for different temperatures. Coloured solid lines encode numerical results. Blue, red and green refer respectively to 25, 60 and 85 °C. Black symbols encode measured data. Circle, star and triangle refer respectively to 25, 60 and 85 °C. Solid black lines are interpolating curves passing through the first two symbols above threshold. Right: modal gain as a function of the carrier density at threshold for the three different temperatures. Black horizontal line represents threshold modal gain.

On the contrary, a very good matching is obtained for high bias when thermal roll-over appears. Fitting is achieved changing the shape of η_i varying T_{th} and
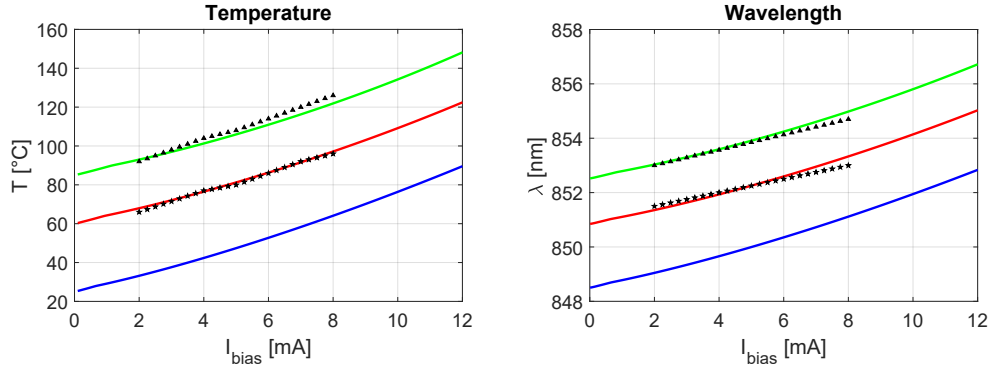
Figure 3.5. Left: temperature against current for different temperatures. Right: wavelength against current for different temperatures. Blue, red and green refer respectively to 25, 60 and 85 ℃. Black symbols encode measured data. Star and triangle refer respectively to 60 and 85 ℃.
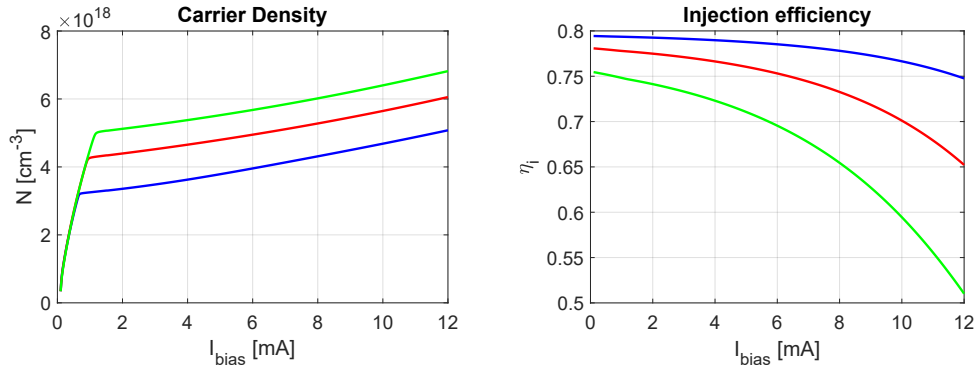

Figure 3.6. Left: carrier density versus current for different temperatures. Right: injection efficiency against current for different temperatures. Blue, red and green refer respectively to 25, 60 and 85 ℃.

$T_{1/2}$; the final $\eta_i(T)$ behaviour is visible in Figure 3.6, right. For all the initial temperatures, output power droop happens when the internal efficiency is lower than 0.7, approximatively a decrease of $\approx 10\%$ from the initial value 0.8. So, the injection efficiency reduction, as a function of temperature, lowers the LI average slope efficiency from 0.48 W/A (25 ℃) to 0.34 W/A (85 ℃). It would be of interest having some measures of η_i to understand exactly if this is the most important parameter to determine roll-over in such bias range. As stated in Chapter 2, the decrease of photon lifetime must be too strong to determine a droop in the output power. In fact, output power is inversely proportional to the photon lifetime: decreasing τ_p increases P_{out}. In order to have a reduction of the output power, photon lifetime must increase the threshold gain such as the corresponding threshold

34

carrier/current density is very high. For this reason, photon lifetime variation is neglected imposing $T_{\tau_p} = \infty$. It is important to remind that, as a consequence, the absorption losses, and so the optical efficiency η_O, are kept constant against temperature and bias. The constant value of the photon lifetime used has been taken from other simulations provided by TRUMPF obtained from more sophisticated models. The same happens for Γ that is generated by a 1D optical mode solver based on coupled-mode theory whose input is the epitaxial structure of the device. The need of advanced extra-model or extra-measurements indicates the weakness of such simple rate equation model: some parameters must be known a priori and not all the whole set of parameters can be used for fitting pretending to have consistent physical results.

The last parameter η_O is used to fit the slope of LI curve at 25 °C; its value is set constant for all the temperatures since reduction of slope can be attributed to the internal quantum efficiency.

3.2.1 A new parameter: dλ

In the previous section, threshold matching between measurements and results is not achieved due to the gain shape. A new parameter dλ is introduced in the model to obtain a better threshold fit. It represents an offset to the wavelength where gain is evaluated. Let λ_0 be defined as the lasing wavelength stated by measurements. Gain parameters should be extracted at $\lambda = \lambda_0$ but now they are evaluated at $\lambda = \lambda_0 + d\lambda$. The effect is a variation in the behaviour of the threshold versus temperature. Figure 3.7 shows I_{th} and N_{th} against temperature for different values of dλ. Considering no offset (blue curve) the threshold current has a very huge increase that does not follow the measurements where the maximum I_{th} is 0.73 mA at 85 °C. Increasing dλ is possible to have a smoother behaviour introducing a minimum of the threshold current around 50 °C (yellow curve). The idea to have a threshold fairly constant versus temperature follows the aim to have a temperature-independent laser. A better fit could be achieved using dλ = 7 nm.

Figure 3.8, right, shows a comparison between the old gain-LUT curves with dλ = 0 (dashed curves) and the new one with dλ = 7 nm (solid curves). Blue, red and green colours refer to 25, 60 and 85 °C, respectively. Dashed curves are evaluated at the wavelength near threshold with no offset: 848.5 (blue), 851.5 (red) and 852.5 nm (green). Solid curves, instead, are evaluated with an offset of 7 nm: 855.5 (blue), 858.5 (red) and 859.5 nm (green). Dashed curves are equally spaced meaning that they have been affected a lot by temperature and wavelength shifts. On the contrary, the introduction of dλ makes solid curves closer, as expected, so that 25°C (blue) and 60 °C (red) overlap near threshold. It is the wanted temperature-independent behaviour. As a consequence, the corresponding threshold currents are much closer as Figure 3.8, left, demonstrates. Numerical value are summarized in Table 3.2.
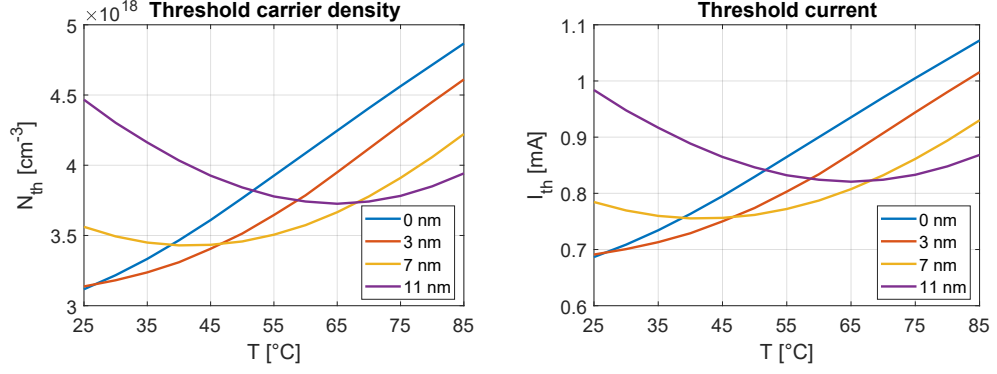
Figure 3.7.   Left: threshold carrier density against temperature for different dλ. Right: the corresponding threshold current. Blue, red, yellow and purple curve refer to different dλ, respectively 0, 3, 7 and 11 nm.
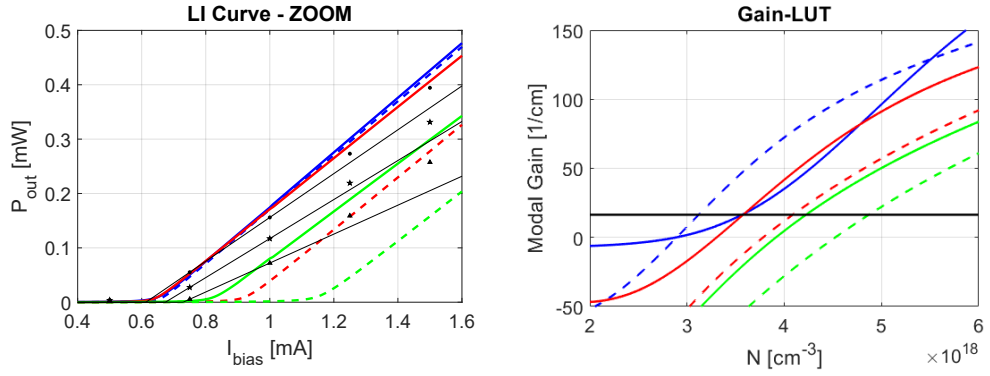

Figure 3.8.   Left: LI curves for different temperatures with d$\lambda = 7$ nm (solid curves) and d$\lambda = 0$ nm (dashed curves). Blue, red and green refer respectively to 25, 60 and 85 °C. Black symbols encode measured data. Circle, star and triangle refer respectively to 25, 60 and 85 °C. Solid black lines are interpolating curves passing through the first two symbols above threshold. Right: the corresponding modal gain against carrier density. Black horizontal line represents the threshold modal gain.

The final LI evaluated with the introduction of $d\lambda$ is shown in Figure 3.9. All the parameters from Table 3.1 remain the same except for τ_c, T_{th} and T_η that are respectively 3 ns, 32 K and 441 K. The first one is changed to match the new threshold and the others to achieve the best fit around the thermal roll-over.

Now, results fit much better both near threshold and thermal roll-over. Fitting quality can be considered enough for such simple model.

T	dλ = 0 nm	dλ = 7 nm	Measure
25 °C	0.67	0.65	0.61
60 °C	0.92	0.65	0.67
70 °C	1.00	0.70	0.71
85 °C	1.15	0.82	0.73

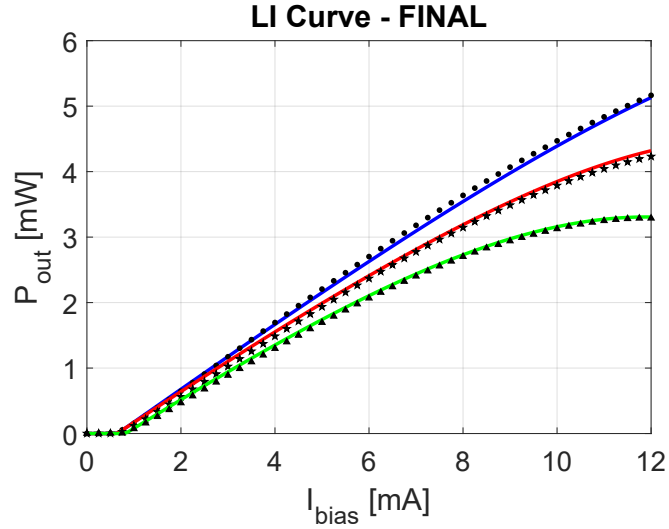Table 3.2.   Threshold current (mA).

Figure 3.9.   LI curve for different temperature using dλ = 7 nm. Blue, red and green refer respectively to 25, 60 and 85 °C. Black symbols encode measured data. Circle, star and triangle refer respectively to 25, 60 and 85 °C.

3.3   Small signal response

The device under test has been developed to be adopted in a communication link aiming to reach 25 Gb/s. The prediction of modulation speed, clearly, gives a great relevance to the dynamic analysis. The measurements taken into account for dynamic analysis are the one related to the scattering parameters S_{11} and S_{21}. From the first, it is possible to extract parasitics by means a de-embedding procedure as shown in Chapter 2. Values are not shown since they are confidential results. From the second, it is possible to extract some relevant figures of merit as the resonance frequency and the damping factor.

The intrinsic small signal response of a laser is a second order type response that
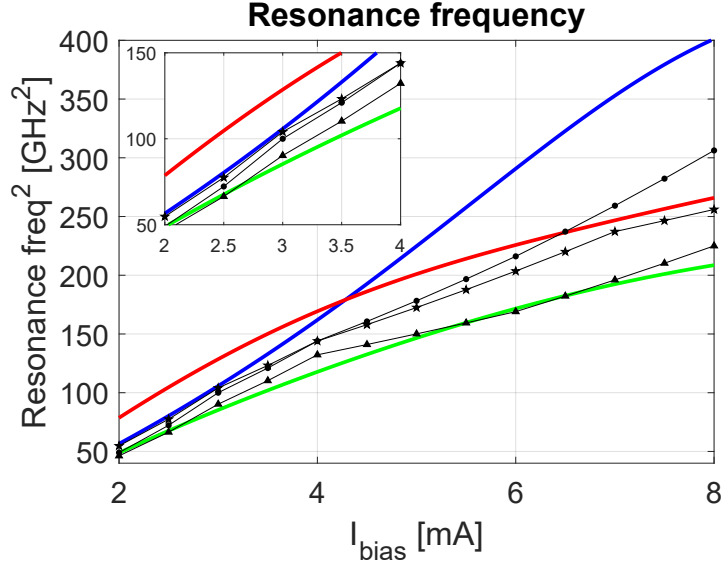
Resonance frequency

Figure 3.10.   Square of the resonance frequency versus current for different temperatures. The inset shows a zoom around 2 and 4 mA. Coloured solid lines encode numerical results. Blue, red and green refer respectively to 25, 60 and 85 °C. Black symbols encode measured data. Circle, star and triangle refer respectively to 25, 60 and 85 °C. Solid black lines are interpolating curves passing through them.

can be expressed as

$$H_{int}(\omega) = \frac{\omega_R^2}{\omega_R^2 - \omega^2 + j\omega\gamma} \tag{3.1}$$

where ω_R is the relaxation frequency and γ the damping factor. Fixing both parameters, the intrinsic dynamic response is defined. So, from the S_{21} measurements, eliminating the contribution of the parasitics, it is possible to extract ω_R and γ for each bias and each temperature. Therefore, interpolating them, graphs that summarize the global dynamic behaviour of the device can be created. It is of interest to represent the square of the resonance frequency versus the current and the damping factor versus the square of the resonance frequency since both show a linear dependence. Simulations are compared with the one taken from S_{21} measurements in Figure 3.10 and 3.11. These results take into account the introduction of dλ = 7 nm. The range of current of interest is the one used to bias the device, far from threshold and far from thermal roll-over. For what concern resonance frequency in Figure 3.10, simulated results show an higher ω_R for blue curve (25 °C) and for high bias, a good fit for red curve (60 °C) and an optimum fit for the green one (85 °C). It is appreciable around 4 mA a cross between blue (25 °C) and red curve (60 °C) both in measurements and simulation results. This result gives more relevance to the goodness of the adoption of dλ. Indeed, as Figure 3.12
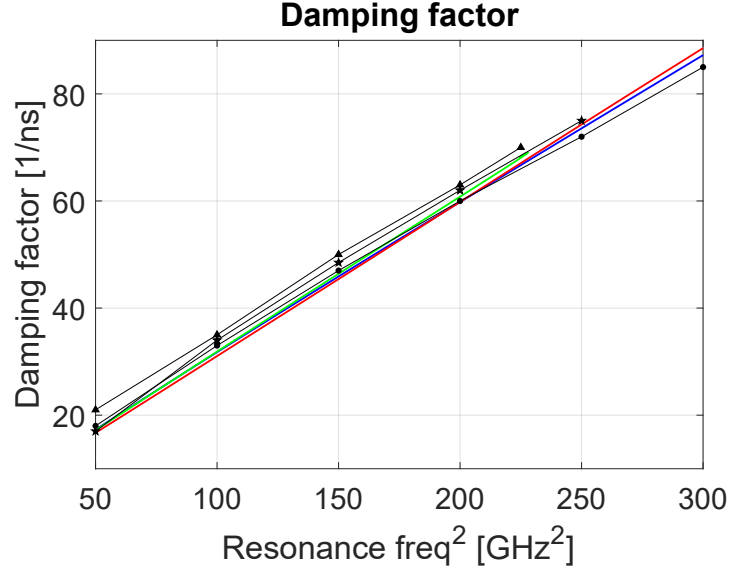
Damping factor

Figure 3.11. Damping factor versus the square of resonance frequency. Coloured solid lines encode numerical results. Blue, red and green refer respectively to 25, 60 and 85 °C. Black symbols encode measured data. Circle, star and triangle refer respectively to 25, 60 and 85 °C. Solid black lines are interpolating curves passing through them.

justifies, setting the wavelength offset to zero the cross is no more present between blue and red curves since the three coloured solid lines are equally spaced.

For what concerns damping factor, shown in Figure 3.11, the independent behaviour of γ is respected in simulations: all the curves more or less overlap each others.

A global perfect fit is very complex to be achieved since rate equation model is very simple. Furthermore, the device under test, in the bias range of interest, has many lasing modes.

It is key to understand which parameter affects the behaviour of ω_R and γ. It helps to use analytical formulas. They can be considered correct since numerical results match analytical formulas for what concerns the dynamic analysis. Above threshold

$$\omega_R^2 = v_g a \frac{N_p}{\tau_p} = v_g a \frac{P_{out}\Gamma}{Vhf\eta_O} \tag{3.2}$$

with

$$a = \frac{a_0}{1 + \epsilon N_p} \tag{3.3}$$

where a_0 is the differential gain evaluated in the corresponding bias point. Not
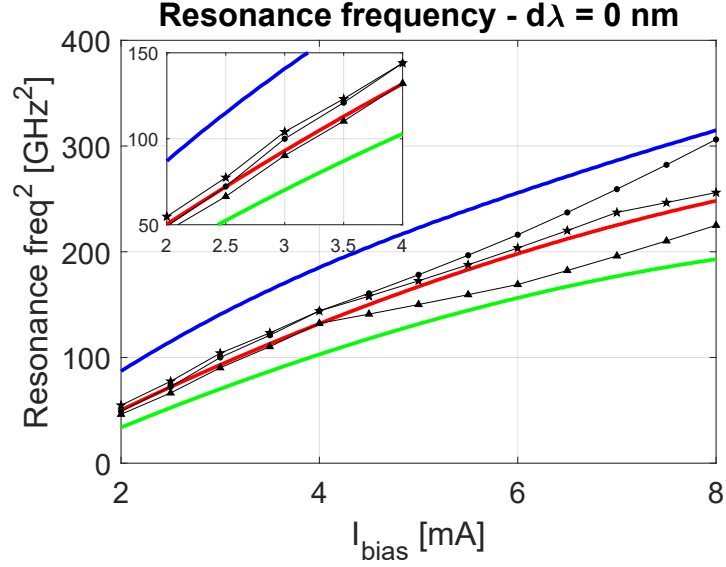
Figure 3.12. Square of the resonance frequency versus current with $d\lambda = 0$ nm. The inset shows a zoom around 2 and 4 mA. Coloured solid lines encode numerical results. Blue, red and green refer respectively to 25, 60 and 85 ℃. Black symbols encode measured data. Circle, star and triangle refer respectively to 25, 60 and 85 ℃. Solid black lines are interpolating curves passing through them.

considering the differential gain, the only factors that change with the current are P_{out} and f. Since the frequency variation is very small, the overall behaviour of ω_R should be linear for all the temperature and not only for 25 ℃ since it is dictated by the output power that is linear in the considered range. As a consequence, the differential gain is the only factor that can decrease so much the variation versus the current of the square of the resonance frequency. Figure 3.13 shows the behaviour of a and a_0 as a function of the current. Only at 25 ℃ an increasing behaviour is observed for low bias, while the other two curves show a monotonically decreasing trend. Differential gain limits the bandwidth for high bias. Setting ϵ is to zero (dashed curves), the behaviour of the intrinsic differential gain of the active material a_0 can be appreciated. It also decreases with high current/temperature limiting the device intrinsic bandwidth. Clearly, at higher current (> 8 mA) P_{out} starts to decrease limiting the modulation speed of the laser too.

For what concerns the fitting procedure, in order to match measured datas, the parameters F defining the volume (2.33) has been used as a fitting parameter. Figures 3.10 and 3.11 show results for $F = 2$, the same value used for LI curve evaluation. Without the presence of F (setting $F = 1$) it would be not possible to have a reasonable fit as Figure 3.14 demonstrates. Indeed, no matching is obtained between coloured (numerical) and black (measures) curves. The introduction of $F = 2$ makes possible the volume to be doubled so that the square resonance
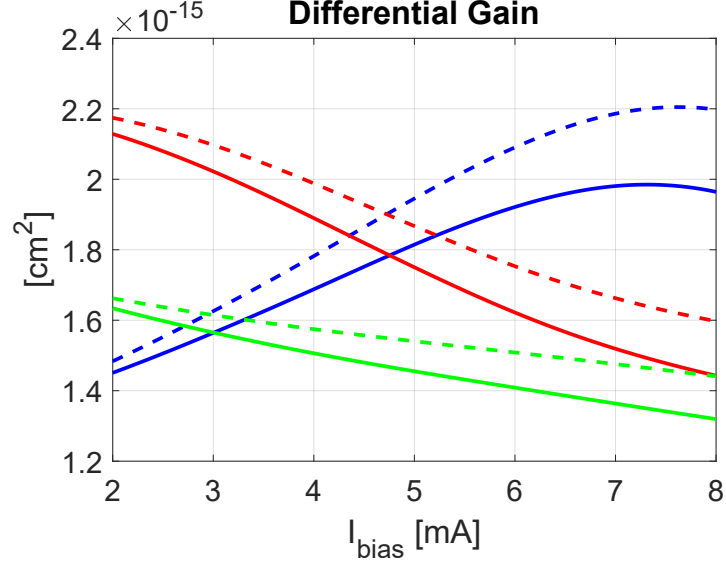
Figure 3.13. Differential gain a (solid curves) with gain compression factor and differential gain a_0 (dashed curves) without gain compression factor versus current for different temperatures. Blue, red and green refer respectively to 25, 60 and 85 °C.

frequency halves as stated from equation 3.2. Physically, it suggests that carriers are spreading after the oxide aperture reaching the active region with an increased area lowering the performance.

The next step is to analyse the damping factor behaviour. Above threshold,

$$\gamma = K f_R^2 + \gamma_0 \tag{3.4}$$

where

$$K = 4\pi^2 \tau_p \left(1 + \frac{\Gamma a_p}{a} \right) \qquad \gamma_0 = \frac{1}{\tau_{\Delta N}} + \frac{\Gamma^2 \beta_{sp} B N_0^2}{N_{p0}} \tag{3.5}$$

and

$$a_p = \left. \frac{\partial g}{\partial N_p} \right|_{N_p} = \frac{\epsilon}{1 + \epsilon N_p} \tag{3.6}$$

The only parameter that can be changed to fit the damping factor is the gain compression factor ϵ. This latter has a direct impact on the definition of γ since both measure the height of the amplitude peak in the small signal response. The damping factor also depends on other parameters such as Γ and τ_p, but they have already been fixed to match all the previous fits. Since the analysed device shows a
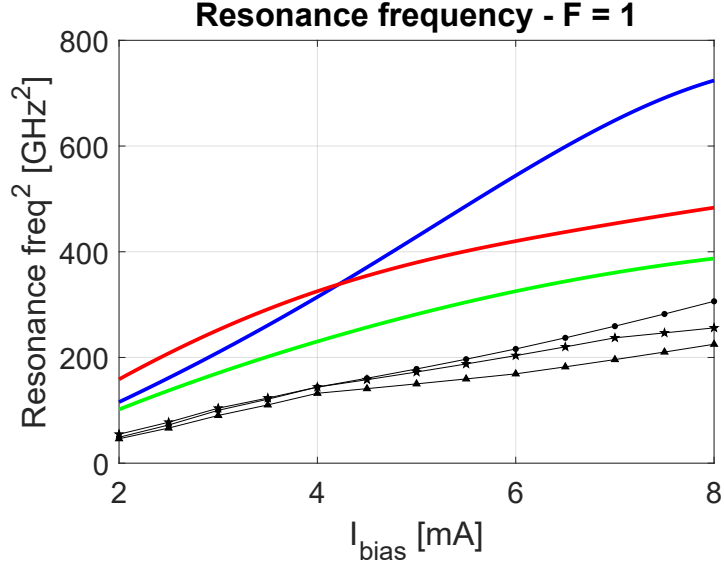
41

Figure 3.14. Square of the resonance frequency versus current with $F = 1$. Coloured solid lines encode numerical results. Blue, red and green refer respectively to 25, 60 and 85 °C. Black symbols encode measured data. Circle, star and triangle refer respectively to 25, 60 and 85 °C. Solid black lines are interpolating curves passing through them.

temperature-independent behaviour for γ, a parametric analysis of ϵ is performed only at 25 °C. Figure 3.15, right, shows an increase of the damping factor as ϵ increases with a good match for $\epsilon = $ 2E-17 cm^3. The behaviour of the four curves is the one expected: higher gain compression factor due to spectral hole burning or carrier transport effect limits more and more the frequency response making it more damped. For high bias, the overall response is dictated predominantly by γ with respect to ω_R. The variation on ϵ does affect the resonance frequency as shown in Figure 3.15, left. It seems that higher ϵ guarantees a better match but it is not completely true for two reasons. On one hand, choosing higher ϵ (purple curve) damping factor does not follow the measurements (black curve). On the other hand, looking at ω_R, also other temperatures (60 °C and 85 °C) will be affected by the bigger ϵ and the good matching previously obtained for $\epsilon = $ 2E-17 cm^3 would be lost. So $\epsilon = $ 2E-17 cm^3 remains a good trade-off between resonance frequency and damping fitting.

The previous considerations show a global view of the intrinsic small response by means of two main parameters γ and ω_R. It is also important to give a look to a local comparison between the numerical $H(\omega)$ and the measured one. Results are illustrated in Figure 3.16. The numerical transfer function shown is the total one that takes into account also parasitics. Bias points chosen are the one of interest: where the device will be biased for a direct modulation. Results agree with all the
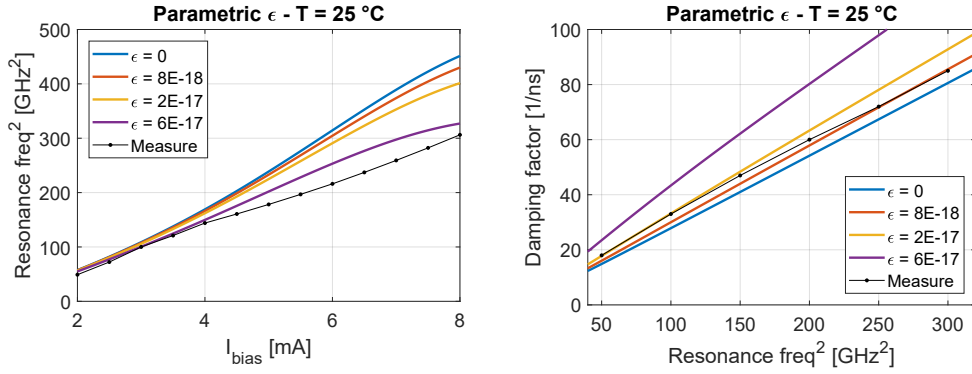
Figure 3.15. Left: square of the resonance frequency versus current at 25°C for various ϵ. Right: the corresponding damping factor. Coloured lines encode numerical results. Black circle refers to measure at 25 °C. Solid black line is an interpolating curve passing through them.
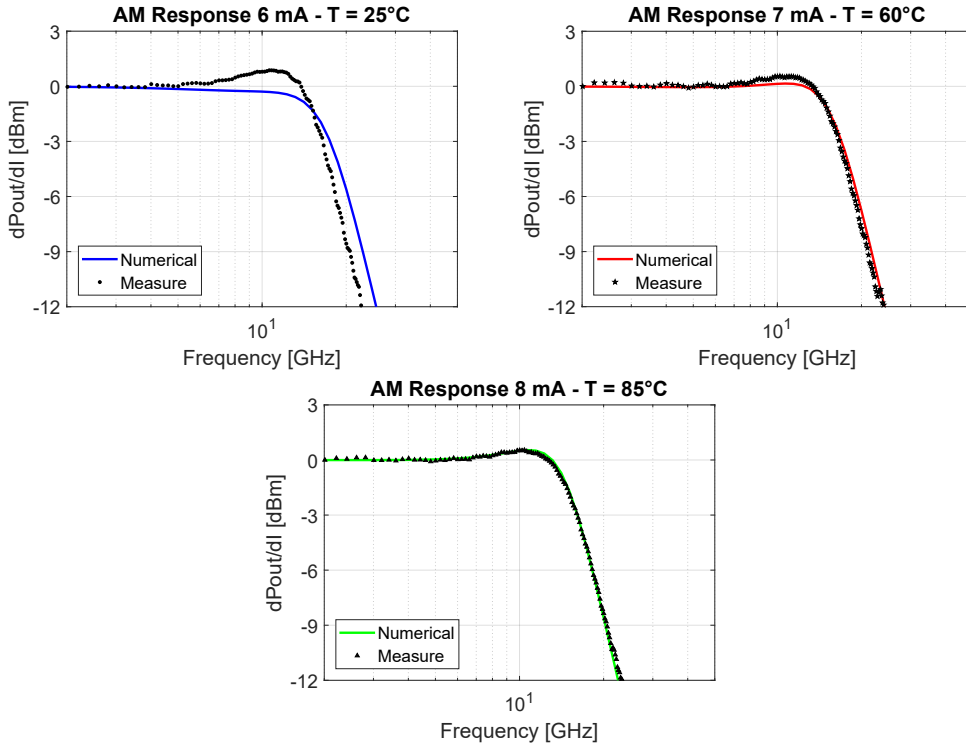
previous considerations.

Figure 3.16. Top left: transfer function at 25 °C and 6 mA (blue). Top right: transfer function at 60 °C and 7 mA (red). Down: transfer function at 85 °C and 8 mA (green). Black symbols encode measured data.

At system level, the main parameter of interest is the -3dB bandwidth. Figure 3.17 shows it against current for different temperatures with and without the parasitics circuit. A fit can be obtained only considering parasitics (solid curves). They affect dramatically the modulation capability that could be higher than 50% (dashed curves). Considering solid lines, a global good match is obtained only for 85 °C: it is expected due to the fit of Figure 3.10. Generally, the bandwidth evaluated numerically at 25 °C and 60 °C is higher with respect to the measured one with a maximum error of the $\approx$ 20 %. At 7 mA and 8 mA a good matching is obtained for all the three temperatures since here the bandwidth is determined by the damping factor that, as stated before, shows a good match with measurements.
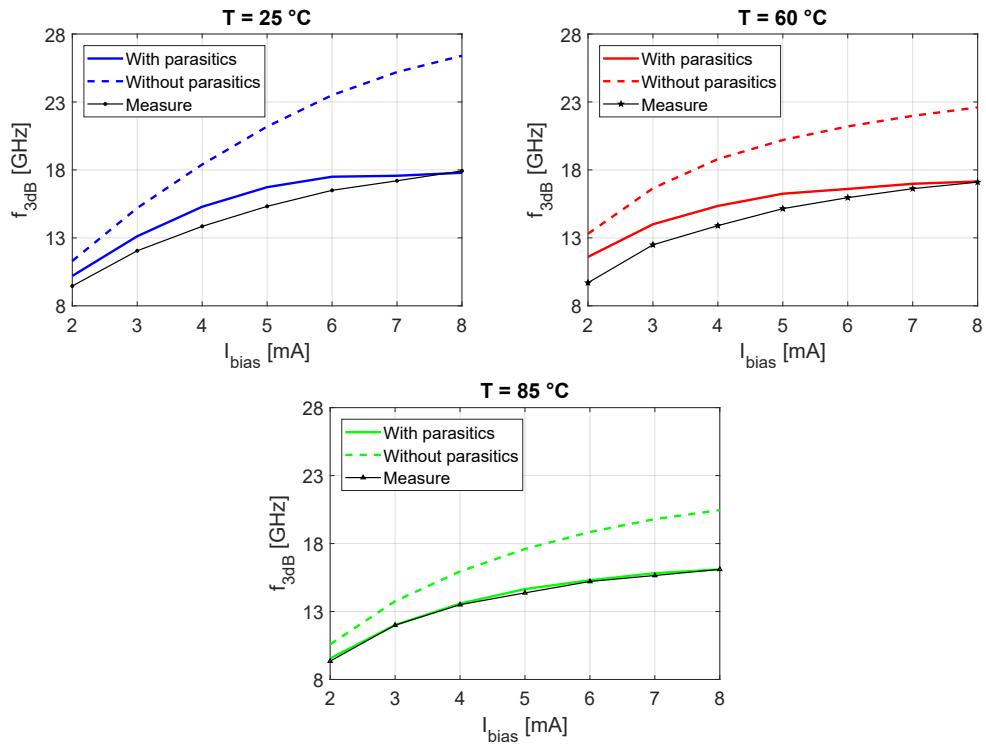

Figure 3.17. Top left: 3dB bandwidth at 25 °C (blue). Top right: 3dB bandwidth at 60 °C (red). Down: 3dB bandwidth at 85 °C (green). Solid coloured curves refer to the bandwidths with parasitics, dashed ones refer to the intrinsic bandwidth without parasitics. Black symbols encode measured data. Solid black lines are interpolating curves passing through them.

3.4   Spline VS logarithmic interpolation

Chapter 2 described the logarithmic fit used during the simulations. In this section, it is compared with spline interpolation, one of the most accurate fitting technique. Two simulations are performed, one based on logarithmic fit and the other one on spline. Both simulations have the same mesh points and use exactly the same algorithmic. The only differences are related to the extraction of the gain shape and the evaluation of the gain. To derive the gain shape in the spline case, a system inversion must be performed, whose size is determined by the number of interpolating points in order to extract all the coefficients to define the spline. Instead, two analytical formulas must be evaluated in the logarithmic case to find out g_0 and N_{tr}. Once the gain shape is set, in the Runge-Kutta solver, in each point of the time window a piecewise polynomial of the 4th order is evaluated in the spline case ($g = \mathrm{ppval}(\mathrm{spline}, N)$) and a logarithmic in the other case ($g = g_0 \log \frac{N}{N_{tr}}$). Figures 3.18 and 3.19 show, respectively, a comparison on the LI curve and on ω_R using the two different interpolation techniques. They match perfectly as a demonstration of the high quality of the logarithmic fitting. Average relative error between solid and dashed curves is of the order of 0.01 %.

   In order to verify the power of the logarithmic interpolation technique, a look to the execution times of both algorithms is needed. The processor used for the simulation is an Intel Core i5-5200U (2 core). The results, for each temperature using a mesh of 271 bias points and 1000 time points for Runge-Kutta solver, are summarized in Table 3.3. Logarithmic algorithm is approximatively twenty times faster than the spline one. Higher computational time for spline is related to the evaluation of gain with the 'ppval' routine since it is performed for each bias and for each time in the Runge-Kutta solver. As shown, a very simple analytical model can significantly reduce simulation times providing the same results of a more complex interpolation algorithm.

T	Log	Spline
25 °C	28 s	535 s
60 °C	29 s	555 s
85 °C	38 s	656 s

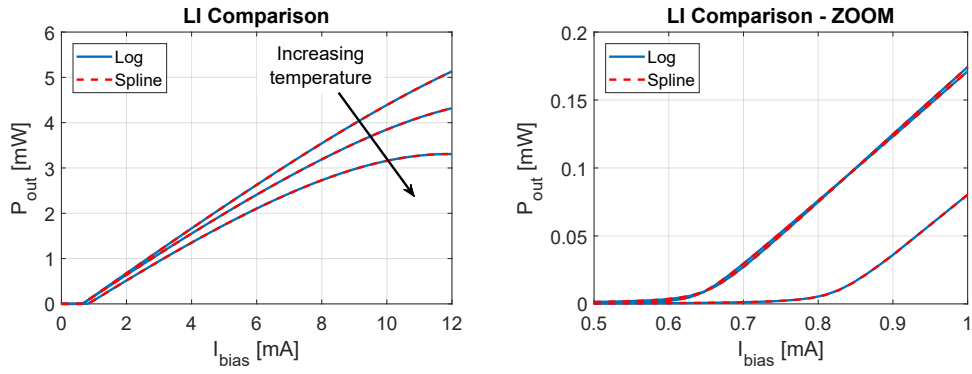Table 3.3.   Execution time for logarithimc and spline fit.

Figure 3.18. Left: LI comparison logarithmic versus spline fit for T = [25, 60, 85] °C. Right: LI zoom near threshold.
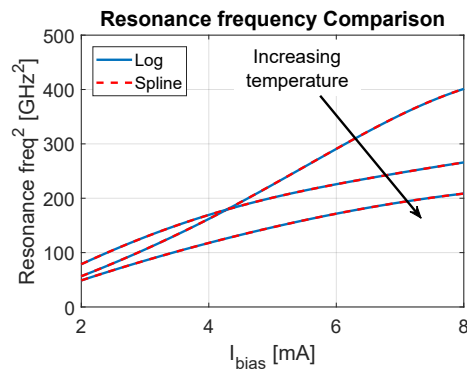

Figure 3.19. Square of the resonance frequency: logarithmic versus spline fit for T = [25, 60, 85] °C.

Chapter 4

Conclusions

4.1 Conclusions

This work focused on the implementation of a temperature-dependent rate-equation model for VCSELs. The idea was to start from a commonly adopted rate equation model, whose analytical solution is known, and to introduce a simple model for thermal effects that are relevant in real devices. The addition of temperature highlighted the need for a more accurate model for the optical response of the active region. So in light of this, particular attention has been given to the modelling of the gain. Its variation induced by temperature was not enough to model the characteristic power droop of real devices. Therefore, a phenomenological temperature-dependent model for the injection efficiency has been introduced.

Application of the implemented model to real devices showed the way for the introduction of new parameters. Gain shape greatly affected the threshold current so that a new parameter $d\lambda$ has been introduced in the model to achieve a good fit near threshold. It stressed the importance of having a particular material in the active region to reach a temperature-independent behaviour. The adoption of another new parameter F, modelling the active region volume, has been relevant to reach a fit for what concern dynamic analysis. It suggested that, in the device under test, carriers are spreading after the oxide aperture reaching the active region with an increased area lowering the performance. Above all, the parasitics have been the main limiting factor in the modulation performance.

The proceeding analysis has been appealing due to its simplicity but still providing intuitive insights. On one hand, the model has been able to identify the main limiting factors of the performance: the injection efficiency for static analysis and the parasitics for the dynamic one. On the other hand, the model has been also able to show the effect of a particular material as active region, through gain and differential gain, on figures of merit, such as the threshold current and the resonance frequency. It is key to highlight that the real device used was a multimodal one while the model is simply single mode. At the end, agreements with experimental

results can be considered enough for such simple model that also showed a fast execution time.

It would have been interesting to have some measures on the gain to verify the introduction of dλ and on the internal efficiency to test the phenomenological approach adopted.

4.2   Future scenario

Stemming from this work, the model could be used to simulate a direct large signal modulation in a TX/RX (transmitter/receiver) system with different modulation schemes in order to obtain eye diagrams relevant from a telecommunication point of view.

Bibliography

[1] Haruhisa Soda, Ken ichi Iga, Chiyuki Kitahara, and Yasuharu Suematsu. GaInAsP/InP surface emitting injection lasers. *Japanese Journal of Applied Physics*, 18(12):2329–2330, dec 1979.

[2] Jim A. Tatum, Andrew Clark, James K. Guenter, Robert A. Hawthorne III, and Ralph H. Johnson. Commercialization of Honeywell's VCSEL technology. In Kent D. Choquette and Chun Lei, editors, *Vertical-Cavity Surface-Emitting Lasers IV*, volume 3946, pages 2 – 13. International Society for Optics and Photonics, SPIE, 2000.

[3] B. Tell, Y. H. Lee, K. F. Brown-Goebeler, J. L. Jewell, R. E. Leibenguth, M. T. Asom, G. Livescu, L. Luther, and V. D. Mattera. High-power cw vertical-cavity top surface-emitting gaas quantum well lasers. *Applied Physics Letters*, 57(18):1855–1857, 1990.

[4] Faces light up over vcsel prospects. *SPIE*, 9 April 2018.

[5] Intel made smart glasses that look normal. *The Verge*, 5 February 2018.

[6] R. S. Geels, S. W. Corzine, J. W. Scott, D. B. Young, and L. A. Coldren. Low threshold planarized vertical-cavity surface-emitting lasers. *IEEE Photonics Technology Letters*, 2(4):234–236, 1990.

[7] M. Orenstein, A. C. Von Lehmen, C. Chang-Hasnain, N. G. Stoffel, J. P. Harbison, L. T. Florez, E. Clausen, and J. E. Jewell. Vertical-cavity surface-emitting InGaAs/GaAs lasers with planar lateral definition. *Applied Physics Letters*, 56(24):2384–2386, 1990.

[8] C. Cheng, N. Ledentsov, Z. Khan, J. Yen, N. N. Ledentsov, and J. Shi. Ultra-fast zn-diffusion and oxide-relief 940 nm vertical-cavity surface-emitting lasers under high-temperature operation. *IEEE Journal of Selected Topics in Quantum Electronics*, 25(6):1–7, 2019.

[9] A. Black, A. R. Hawkins, N. M. Margalit, D. I. Babic, A. L. Holmes, Y. . Chang, P. Abraham, J. E. Bowers, and E. L. Hu. Wafer fusion: materials issues and device results. *IEEE Journal of Selected Topics in Quantum Electronics*, 3(3):943–951, 1997.

[10] M. Verplaetse, L. Breyne, C. Neumeyr, T. De Keulenaer, W. Soenen, X. Yin, P. Ossieur, G. Torfs, and J. Bauwelinck. Dsp-free and real-time nrz transmission of 50gb/s over 15km ssmf and 64gb/s back-to-back with a 1.3μm vcsel. In

2018 Optical Fiber Communications Conference and Exposition (OFC), pages 1–3, 2018.

[11] R. P. Schneider and J. A. Lott. Cavity design for improved electrical injection in inalgap/algaas visible (639–661 nm) vertical-cavity surface-emitting laser diodes. *Applied Physics Letters*, 63(7):917–919, 1993.

[12] E. Haglund, P. Westbergh, J. S. Gustavsson, E. P. Haglund, A. Larsson, M. Geen, and A. Joel. 30 ghz bandwidth 850 nm vcsel with sub-100 fj/bit energy dissipation at 25–50 gbit/s. *Electronics Letters*, 51(14):1096–1098, 2015.

[13] Daniel M. Kuchta, Alexander V. Rylyakov, Clint L. Schow, Jonathan E. Proesel, Christian W. Baks, Petter Westbergh, Johan S. Gustavsson, and Anders Larsson. A 50 Gb/s NRZ modulated 850 nm vcsel transmitter operating error free to 90 °c. *J. Lightwave Technol.*, 33(4):802–810, Feb 2015.

[14] S. T. M. Fryslie, M. P. T. Siriani, D. F. Siriani, M. T. Johnson, and K. D. Choquette. 37-ghz modulation via resonance tuning in single-mode coherent vertical-cavity laser arrays. *IEEE Photonics Technology Letters*, 27(4):415–418, 2015.

[15] Zhongwei Tan, Chuanchuan Yang, Yixiao Zhu, Zhaopeng Xu, Kaiheng Zou, Fan Zhang, and Xiao Chen. A 70 gbps nrz optical link based on 850 nm band-limited vcsel for data-center intra-connects. *Science China Information Sciences*, 61:080406, 02 2018.

[16] F. Karinou, N. Stojanovic, C. Prodaniuc, Z. Qiang, and T. Dippon. 112 gb/s pam-4 optical signal transmission over 100-m om4 multimode fiber for high-capacity data-center interconnects. In *ECOC 2016; 42nd European Conference on Optical Communication*, pages 1–3, 2016.

[17] Smartphone market pulls vcsels into the mainstream. *physicsworld*, 23 Aug 2019.

[18] A. Tibaldi, F. Bertazzi, M. Goano, R. Michalzik, and P. Debernardi. Venus: A vertical-cavity surface-emitting laser electro-opto-thermal numerical simulator. *IEEE Journal of Selected Topics in Quantum Electronics*, 25(6):1–12, 2019.

[19] Alberto Tibaldi, Francesco Bertazzi, Michele Goano, Rainer Michalzik, and Pierluigi Debernardi. Venus: A vertical-cavity surface-emitting laser electro-opto-thermal numerical simulator. *IEEE Journal of Selected Topics in Quantum Electronics*, PP:1–1, 01 2019.

[20] P. Debernardi. Hot-velm: A comprehensive and efficient code for fully vectorial and 3-d hot-cavity vcsel simulation. *IEEE Journal of Quantum Electronics*, 45(8):979–992, 2009.

[21] Masumi Takeshima. Effect of auger recombination on laser operation in ga1-xalxas. *Journal of Applied Physics*, 58(10):3846–3850, 1985.

[22] Jeng-Ya Yeh, L. J. Mawst, and N. Tansu. The role of carrier transport on the current injection efficiency of ingaasn quantum-well lasers. *IEEE Photonics Technology Letters*, 17(9):1779–1781, 2005.

[23] Rainer Michalzik. In *Fundamentals, Technology and Applications of Vertical-Cavity Surface-Emitting Lasers*, volume 166.